

Lawrence Berkeley National Laboratory

Lawrence Berkeley National Laboratory

Title

SINGLE ELECTRON ATTACHMENT AND STRIPPING CROSS SECTIONS FOR RELATIVISTIC HEAVY IONS

Permalink

<https://escholarship.org/uc/item/4qt0h4bz>

Author

Crawford, H.J.

Publication Date

1979-06-01

Peer reviewed

Single Electron Attachment and Stripping Cross Sections for Relativistic Heavy Ions

Henry J. Crawford

University of California at Berkeley

ABSTRACT

We report the results of a Bevalac experiment to measure the single electron attachment and stripping cross sections for relativistic ($0.5 < \beta < 0.95$) C, Ne and Ar ions passing through thin solid targets ranging in atomic number from 4 (Be) to 79 (Au). Magnetic analysis was used to separate the single electron, N_1 , and fully stripped, N_0 , ion beams emerging from the targets. Separate counters measured the number of ions in each charge state. The ratios N_1/N_0 for different target thicknesses were fit to a simple growth curve to yield electron attachment and stripping cross sections. The data are compared to relativistic extrapolations of available theories. Clear evidence for two separate attachment processes, radiative and non-radiative, is found. Data are compared to a recently improved formulation for the stripping cross sections.

This report was prepared with the support of the U. S. Department of Energy under Contract No. W-7405-ENG-48.

DISCLAIMER

This book was prepared as an account of work sponsored by an agency of the United States Government. Neither the United States Government nor any agency thereof, nor any of their employees, makes any warranty, express or implied, or assumes any legal liability or responsibility for the accuracy, completeness, or usefulness of any information, apparatus, product, or process disclosed, or represents that its use would not infringe privately owned rights. Reference herein to any specific commercial product, process, or service by trade name, trademark, manufacturer, or otherwise does not necessarily constitute or imply its endorsement, recommendation, or favoring by the United States Government or any agency thereof. The views and opinions of authors expressed herein do not necessarily state or reflect those of the United States Government or any agency thereof.

REPRODUCTION OF THIS DOCUMENT IS UNLIMITED

Fig

Table of Contents

I. Introduction	
A. General Description	1
B. Experimental Method	2
C. Growth Curve	2
D. Theory	6
1. Electron Attachment	7
a. Radiative	7
b. Non-Radiative	11
c. Excited States	14
2. Electron Stripping	14
E. Scope of Data	18
II. Experimental Details	
A. Introduction	20
B. Bevalac	20
C. Targets	21
D. Spectrometer	22
E. Beam Monitor	24
F. Signal Monitor	25
G. Data Collection	27
H. Backup Experiment	28
III. Analysis	
A. Introduction	30
B. Determination of Beam Fluence, N_0	31
C. Determination of N_1	32
D. Background	33
E. Determination of N_1/N_0	33

F. Targets	34
G. Determination of R_{eq}	34
H. Determination of σ_a and σ_s	35
J. Confidence Levels	36
K. Beam Energy	37
IV. Results and Discussion	
A. Introduction	38
B. Equilibrium Ratios	38
C. Attachment Cross Sections	40
D. Stripping Cross Sections	43
V. Conclusions	45

Single Electron Attachment and Stripping Cross Sections for Relativistic Heavy Ions

Henry J. Crawford

University of California at Berkeley

I.A. Introduction

As an ion traverses matter, its charge state fluctuates as a result of interactions in which it captures or loses electrons. The rate at which these charge fluctuations occur depends strongly on the charge and velocity of the ion and on the atomic number and density of the matter. The processes of electron attachment and stripping have been extensively studied both experimentally and theoretically. Motivation for these investigations is provided by the many practical applications which involve charge-changing interactions and by the diverse theoretical problems involved in calculating cross sections for these processes. However, virtually all of the experimental data on charge exchange cross sections for heavy ions have been limited to velocities $\beta < 0.05$. Such data have been used to develop theoretical and phenomenological formulations for both capture and loss cross sections which work well in low velocity regimes.

The lack of experimental data at higher energies is due primarily to limitations imposed by available heavy ion accelerators rather than to lack of interest. Applications at high velocity include design of heavy ion accelerators and determination of the conditions under which cosmic rays propagate throughout the Galaxy. Theoretical formulations of the problem are most easily made for ions passing through matter at high velocities, that is, velocities which are much greater than the K-shell electron velocities of either the ion or medium. Measurements of these cross sections for very high energy heavy ions could be used to test relativistic quantum electrodynamics by probing the high momentum tails of bound electron wave functions.

When the Lawrence Berkeley Laboratory Bevalac began producing relativistic heavy ion beams it became possible to make measurements in a velocity regime where charge exchange

calculations had never been tested. We have performed an experiment at the Bevalac to measure attachment and stripping cross sections for beams of C, Ne and Ar ions covering the energy range from 140 to 2100 MeV/nucleon. Attachment cross sections derived from our data are compared to calculations for both radiative and nonradiative attachment processes. Stripping cross sections are compared to calculations based on modifications of the Bohr formulae for single electron stripping processes.

I.B. Experimental Method

Beams of fully stripped ions were passed through thin, free standing foil targets. Ions emerging from a target were passed through a magnetic spectrometer to separate different charge states (see Sec.II.D). The number of fully stripped ions emerging, N_0 , was obtained from a secondary emission monitor (see Sec.II.E). The number of single electron ions emerging, N_1 , was counted with a solid state detector telescope (see Sec.II.F). The ratio N_1/N_0 was measured as a function of target thickness for each target element (see Sec.III.E). Values of the single electron attachment cross section, σ_a , and the single electron stripping cross section, σ_s , were determined by fitting these ratios to a simple two state growth curve (see Sec.I.C and Sec.III.H). This ratio approaches a limiting value called the equilibrium ratio, R_{eq} , for thick targets. The projectiles, energies and targets used in this experiment are listed in Table 1.

I.C. Growth curve

In this section we discuss the equation (I.C.6) used to derive attachment and stripping cross sections from our data. We base this equation on consideration of the charge state composition of an ion beam traversing homogeneous matter [cf.ref.1]. Thus we neglect the effect of the target foil-vacuum interfaces.

As an ion beam passes through matter the relative number of ions in each charge state can be described by a set of differential equations which require, in an exact treatment, an intimate knowledge of the atomic physics involved. In principle, each eigenstate of the projectile

ion has its own cross section for attachment and stripping. An incident ion may attach an electron into its ground ($1s$) state or into any excited state. An electron captured into an excited state may be stripped before it has a chance to de-excite to the ground state. Thus the set of equations describing the charge state composition of the beam contains terms that account for capture and loss from individual eigenstates and for transitions between eigenstates resulting from spontaneous and induced decays and from absorption of non-ionizing quanta. Additional complications arise when multi-electron processes are considered.

We will consider only single electron and fully stripped ions as contributing significantly to the charge composition of beams in this analysis. This approximation is justified by the fact that our measured ratios of the number of single electron ions, N_1 , to the number of fully stripped ions, N_0 , are all $<10^{-4}$. We periodically checked the population of two electron ions and found that these contribute $<10^{-2}$ of the single electron ion population. In the remainder of this section we will be concerned with the role of excited states of the single electron ions and the complications these excited states introduce in the interpretation of our measurements.

The equations describing the charge composition of the beam can be simplified if the mean decay time from any excited state to the ground state is either much shorter or much longer than the mean time between stripping collisions. In the case in which the target medium is a very rarefied gas, capture and subsequent stripping interactions are well separated in time. Thus all excited states have a chance to decay to the ground state before suffering another interaction. In the case in which the target is a dense medium and the ion is moving at high speed, the mean collision time is short with respect to the decay time. Each state will then form its own independent capture and loss equilibrium.

The relevant quantities that determine whether we can use a simplified set of equations are the lifetimes for excited states of the ion and the average time between ionizing collisions. The lifetimes of excited states of hydrogenic (i.e. single electron) ions can be estimated according to Bohr and Lindhard [ref.2] as

$$\tau = \tau_0 n^5 / Z^4$$

where $\tau_0 = 0.9 \times 10^{-10}$ sec., n is the effective quantum number associated with the ground state of the ion and Z is the atomic number of the ion. For single electron ions, $n \approx 1-2$. Hence lifetimes relevant to this experiment are on the order of 2×10^{-12} sec. for C^{+6} ions to 3×10^{-14} sec. for Ar^{+18} ions.

The average stripping time, i.e. time between ionizing collisions, as seen in the rest frame of the ion is

$$\tau_s = 1/(\gamma\beta c\sigma_s\rho), \quad \text{I.C.2}$$

where β is the ion's speed in the laboratory, $\gamma = (1-\beta^2)^{-1/2}$, c is the speed of light in vacuum, σ_s is the stripping cross section per target atom and ρ is the density of target atoms per cm^3 . Ion speeds in this experiment range from $0.5c$ to $0.95c$. The densities of atoms in the targets are typically $10^{23}/cm^3$. Stripping cross sections range from $10^{-18}cm^2$ for $C + Au$ at 140 MeV/nucleon to $2 \times 10^{-21}cm^2$ for $Ar + Be$ at 1050 MeV/nucleon. Stripping times thus range from 7×10^{-14} sec. to 3×10^{-16} sec. For C and Ne projectiles the stripping time is clearly much shorter than the decay times for excited states, but for Ar projectiles the stripping and decay times are nearly equal.

If we neglect transitions between eigenstates and consider only single electron processes we arrive at the following simplified set of equations to describe the charge state composition of a beam at a position x in a homogeneous target medium:

$$dN_1(i)/dx = N_0\sigma_{01}(i) - N_1(i)\sigma_{10}(i) \quad \text{I.C.3}$$

$$dN_0/dx = \sum_i N_1(i)\sigma_{10}(i) - N_0\sum_i \sigma_{01}(i)$$

where x is the depth of penetration into the target measured in number of target atoms per cm^2 , N_0 = number of fully stripped ions, $N_1(i)$ = number of single electron ions in projectile eigenstate i , $\sigma_{01}(i)$ = cross section per target atom for single electron attachment into state i and $\sigma_{10}(i)$ = cross section for stripping the single electron from state i .

Our experiment is not sensitive to electron attachment into individual eigenstates of the projectile ion. We measure only the sum over all states having an electron attached. That is , we measure $N_1 = \sum_i N_1(i)$. If we sum over i in eqn.I.C.3 we find

$$d\sum_i N_1(i)/dx = N_0 \sum_i \sigma_{01}(i) - \sum_i N_1(i) \sigma_{10}(i) \quad \text{I.C.4}$$

$$dN_0/dx = \sum_i N_1(i) \sigma_{10}(i) - N_0 \sum_i \sigma_{01}(i)$$

In the rarefied gas target limit, the terms $\sum_i N_1(i) \sigma_{10}(i)$ become $\sigma_{10}(1s) \sum_i N_1(i)$ where, $\sigma_{10}(1s)$ signifies the stripping cross section from the ground state of the single electron ion. We introduce an effective stripping cross section for the dense target regime and thus reduce the set of equations to a simplified form similar to the rarefied gas limit.

Incorporating these simplifications, we use the following approximate equations to describe the charge composition of the beam.

$$dN_1/dx = N_0 \sigma_a - N_1 \sigma_s \quad \text{I.C.5}$$

$$dN_0/dx = N_1 \sigma_s - N_0 \sigma_a$$

For clarity, we repeat that we have defined $N_1 = \sum_i N_1(i)$ and $\sigma_a = \sum_i \sigma_a(i)$ to account for capture into all eigenstates of the projectile. We have also introduced an effective stripping cross section σ_s to reduce the equations to this simple form. Equations I.C.5 can be easily solved for the ratio N_1/N_0 as a function of target thickness yielding

$$R = N_1/N_0 = R_{eq} (1 - e^{-\sigma_s x}) \quad \text{I.C.6}$$

where $R_{eq} = \sigma_a/\sigma_s$ is the equilibrium ratio attained at large target thickness.

In the dense target limit each eigenstate establishes its own equilibrium giving a ratio $N_1(i)/N_0 = \sigma_{01}(i)/\sigma_{10}(i)$. Our technique yields a measurement of $R_{eq} = \sum_i \sigma_{01}(i)/\sigma_{10}(i)$.

Our introduction of an effective stripping cross section is valid only if the $\sigma_{10}(i)$ do not depend strongly on i . Measurements of charge state distributions for 8.5 Mev/nucleon Ar ions in Zapon foils by Heckman et al. [ref.3] support this assumption. We note that the theoretical interpretation of this effective stripping cross section is not straightforward since our measurements do not yield stripping cross sections from a single eigenstate of the projectile ion.

Our cross sections are obtained from fits to this simple growth curve using σ_a and σ_s as fitting parameters. This is equivalent to the assumption that we are dealing with a two state system; either the ion has an electron attached or it does not. We note that by using this ratio to obtain our attachment and stripping cross sections we are able to neglect any effects of nuclear fragmentation interactions on the charge composition.

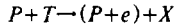
In this experiment we are unable to distinguish effects of individual target eigenstates. Thus, just as our measurement of the attachment cross section represents a sum over excited states of the ion formed, comparison with any theoretical formulation must include an integration over all eigenstates of the target as well.

I.D.Theory

In this section we discuss the equations used to calculate attachment and stripping cross sections for comparison with our data. The problems of electron attachment (or capture) and electron stripping (or loss) are treated separately. Exact calculations of cross sections for these processes are not available. Instead, matrix elements are generally evaluated in the Born approximation or some other perturbation expansion. This approach should be valid when electron velocities are much smaller than the speed of incident ions, i.e. when $\alpha Z/\beta \ll 1$, where Z is the atomic number of either target or projectile ion, β is the relative speed and α is the fine structure constant (we use units in which $\hbar=c=1$). Characteristic values for this parameter for the projectiles and targets used in this experiment are shown in Table 2.

1.D.1. Electron attachment

The process of electron attachment can be represented schematically as

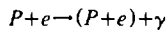


where P is the incident projectile, T is the target supplying the electron, P+e is the single electron ion formed in the interaction and X is present to conserve momentum. When the target is a free electron, X is a photon generated at the instant the electron becomes attached to the projectile. This process is described as radiative electron attachment; the theoretical formulation treats this as the inverse of photoionization. When the target is an atom or a molecule, X represents the recoiling system from which the electron was captured. In this case the process is described as non-radiative attachment.

These two attachment processes have very different velocity dependences. Non-radiative attachment dominates at low velocities but falls as E^{-6} , where E is the energy per nucleon (i.e. velocity) of the incident projectile. One of the motivations for this experiment was to check the β dependence of the non-radiative process, since the best available theories are completely non-relativistic. Radiative attachment falls as E^{-1} and begins to dominate at some energy above a few tens of MeV/nucleon that depends on the atomic number of the projectile and the target.

1.D.1.a. Radiative attachment

This type of reaction is represented schematically as



where P represents the projectile, e the electron, (P+e) the resulting ion and γ the generated photon. In this experiment, a fully stripped projectile nucleus captures a "free" electron to form a single electron ion. A photon is produced in the interaction to satisfy conservation of momentum.

Cross sections for the radiative attachment process can be calculated from photoionization cross sections through the method of detailed balance (cf. Raisbeck and Yiou [ref.4]). In photoionization, a photon is absorbed by an ion with the simultaneous emission of an electron from the ion into the continuum. In radiative electron attachment, an electron is captured by an ion with the simultaneous generation of a photon. The symmetry in these two processes is most easily seen by viewing the interaction in the ion's rest frame in which the electron approaches the ion with speed β , the ion's speed in the lab. We calculate the radiative attachment cross section for an ion of speed β in terms of the photoionization cross section for which an electron is ejected at speed β . Applying detailed balance, which amounts to equating the matrix elements in the two symmetric processes by appealing to time reversal invariance and correcting for the (spin averaged) density of states, we find

$$\sigma_{ra} = 2 \left(\frac{p_\gamma}{p_e} \right)^2 \sigma_\phi Z_T, \quad \text{I.D.1}$$

where σ_{ra} = the radiative attachment cross section per target atom, σ_ϕ = the photoionization cross section per (projectile) ion, p_γ = the momentum of the photon, p_e = the momentum of the "incident" electron and Z_T is the number of electrons per target atom.

The photon energy can be calculated exactly if both the original and the final states consisting of ion and electron are known. The photon energy depends on the electron binding energies in the initial and final states and on the masses of the incident and target ions. As a first approximation we neglect binding effects and assume that the electron was originally free and at rest in the target. Then the photon energy will be nearly equal to the kinetic energy of the electron as seen in the rest frame of the incident ion. Thus $p_\gamma = (\gamma - 1)m_e$ where now $\gamma = (1 - \beta^2)^{-1/2}$. Photon energies in this experiment are greater than 100 keV. Hence we are justified in neglecting binding effects. In this approximation we find

$$\sigma_{ra} = 2 \left(\frac{(\gamma - 1)}{(\beta \gamma)} \right)^2 \sigma_\phi Z_T \quad \text{I.D.2}$$

where we have used the fact that the electron momentum in the ion's rest frame is just $p_e = \beta \gamma m_e$.

Our calculations of σ_{ra} depend directly on our ability to calculate σ_ϕ . Calculations of high energy photoionization cross sections are discussed in a recent review article by Pratt et al.[ref.5]. We require a relativistic treatment of the problem because the photon energies in this experiment are of the same order of magnitude as the electron rest mass.

A relativistic first order Born approximation calculation of σ_ϕ for interactions which lead to ejection of a K-shell electron with speed β from an atom of atomic number Z_p was done by Sauter in 1931 [ref.6], yielding

$$\sigma_\phi = \frac{3}{2} \alpha^4 \sigma_T Z_p^5 \frac{(\beta\gamma)^3}{(\gamma-1)^5} M(\beta), \quad \text{I.D.3}$$

where

σ_T = the Thompson cross section,

β = speed of the ejected electron,

$\gamma = (1-\beta^2)^{-1/2}$ and

$$M(\beta) = \frac{4}{3} + \frac{\gamma(\gamma-2)}{\gamma-1} \left[1 - \frac{1}{2\beta\gamma^2} \ln \frac{1+\beta}{1-\beta} \right].$$

We note that this photoionization cross section assumes there are two K-shell electrons available for ejection in the interaction. Our ions have only a single electron so this cross section must be divided by two before being used to calculate σ_{ra} . Equation I.D.3 is the ionization cross section used by Raisbeck and Yiou [ref.4] to calculate σ_{ra} by equating β with the speed of the incident proton in their experiment.

Pratt et al.[ref.5] discuss modifications of this equation required at high energy for ions of atomic number greater than 1 (cf.discussion by Wilson for the case of electron attachment by high energy cosmic ray nuclei [ref.7]). One modification is to incorporate a calculation to

second order in $\alpha Z/\beta$ performed by Gavrilla [ref.8]. A second modification incorporates Pratt's calculation which uses the distorted wave Born approximation to correct for the influence of the Coulomb field of the projectile on the initial electron wave function [ref.9]. (An additional complication would be to include the effect of the initial binding of the electron.) Taking these corrections into account we arrive at Pratt et al. eqn.6.1.8 [ref.5], the formula which we shall use for the photoionization cross section.

$$\begin{aligned} \sigma_{\phi} = & \frac{3}{2} \alpha^4 \sigma_i Z_p^5 \frac{(\beta\gamma)^3}{(\gamma-1)^5} M(\beta) \\ & \times (\alpha Z_p)^{2\xi} e^{-\frac{\alpha Z_p}{\beta} \cos^{-1}(\alpha Z_p)} \\ & \times [1 + \pi \alpha Z_p \frac{N(\beta)}{M(\beta)} + R(\alpha Z_p)] , \end{aligned} \quad \text{I.D.4}$$

where

$$\xi = -1 + (1 - (\alpha Z_p)^2)^{-1/2} ,$$

$N(\beta)$ = Gavrilla second order correction, $R(\alpha Z_p)$ = a tabulated function, and the remaining quantities are defined for eqn.I.D.3 above. We note that $R(\alpha Z_p) < 10^{-4}$ for all $Z_p < 30$ ([ref.5] Table 6.1) and we therefore neglect this term in all of our calculations.

To calculate the radiative attachment cross section we substitute eqn.I.D.4 in eqn.I.D.2 (dividing by two to account for the single electron present on our ions) and arrive at

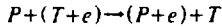
$$\begin{aligned} \sigma_{ra} = & \frac{(\gamma-1)^2}{(\beta\gamma)^2} \frac{3}{2} \alpha^4 \sigma_i Z_p^5 Z_T \frac{(\beta\gamma)^3}{(\gamma-1)^5} M(\beta) \\ & \times (\alpha Z_p)^{2\xi} e^{-\frac{\alpha Z_p}{\beta} \cos^{-1}(\alpha Z_p)} [1 + \pi \alpha Z_p \frac{N(\beta)}{M(\beta)}] , \end{aligned} \quad \text{I.D.5}$$

where β is the speed of the incident ion, $\gamma = (1 - \beta^2)^{-1/2}$, and the remaining quantities are defined for eqns.I.D.3 and I.D.4 above. We note that this equation is for capture of free

electrons into the projectile K-shell (see Sec.I.D.1.c below).

I.D.1.b.Non-radiative attachment

This process can be represented schematically as



where P,T and e are the projectile, target and electron, respectively. If P and T represent fully stripped nuclei there is only one electron involved in the reaction (such as for proton + hydrogen atom). Such an interaction is an example of the general class of transfer or rearrangement collisions [ref.10]. The Hamiltonian for this interaction contains three terms describing the Coulomb interaction between the participants:

$$H = H_0(T,e) + H_1(P,e) + H_2(T,P) \quad \text{I.D.6}$$

where $H_0(T,e)$ accounts for the original binding of the electron in the target atom, $H_1(P,e)$ describes the interaction between the electron and the incident projectile nucleus and $H_2(P,T)$ describes the interaction between the nuclei of the target and projectile. Transition probabilities can be computed by treating the H_1 and H_2 terms as a perturbation on H_0 or by treating H_0 and H_2 as perturbations on H_1 . In either case, if both P and T are nuclei, rather than atoms or ions, the wave functions for the isolated ions which form the basis for the expansion are simple hydrogenic wave functions. In this experiment we did not use hydrogenic targets but we did use fully stripped projectiles.

The non-radiative attachment process is dominant at low ion velocities, the region where most data have been available. The charge changing process for heavy ions at low velocity is complicated, especially for ions traversing solid matter of high atomic number. These complications arise because, at low velocity, the heavy ions typically have many electrons attached. Betz has reviewed this region [ref.11] and discussed the many phenomenological approaches employed to order the data.

The starting point for our formulation of the non-radiative attachment cross sections comes from early work by Oppenheimer [ref.12] and by Brinkman and Kramers [ref.13]. This non-relativistic quantum mechanical treatment, commonly referred to as the OBK approximation, is a calculation of the probability for transfer of an electron from the K-shell of a single-electron target atom to the K-shell of a fully stripped projectile nucleus. The transition probability was calculated in the OBK approximation for a perturbation Hamiltonian that included only the interaction between the electron and the incident nucleus (i.e. H_2 in eqn.I.D.6 was neglected). The non-radiative single electron attachment cross section per target K-shell electron as calculated by Brinkman and Kramers (eqn.4 in their paper) [ref.13] is

$$\sigma_{OBK} = \frac{\pi a_0^2}{5} 2^{18} Z_P^5 Z_T^5 S^8 \quad \text{I.D.7}$$

$$\times [S^2 + (Z_P + Z_T)^2]^{-5} [S^2 + (Z_P - Z_T)^2]^{-5}$$

where $a_0 = 0.529 \times 10^{-8} \text{ cm}$, the Bohr radius ,

Z_P = atomic number of the projectile,

Z_T = effective atomic number of the target, and

$$S = \frac{\beta}{\alpha}.$$

This formula must be multiplied by two for any target having more than one K-shell electron, and Z_T must be corrected [ref.14] to account for deviations of the K-shell wave functions from the simple hydrogenic case [ref.15].

This non-radiative attachment formula is not based on the assumption that the electron was initially free, as is the radiative attachment formulation. It is an explicit calculation for capture from the target K-shell. Our targets are all multi-electron systems. However, at the high velocities used in this experiment we can expect capture from the K-shell to dominate. This is because the amplitude of the high momentum component of the wave functions for higher

shells is much smaller than the amplitude for similar momentum components in the K-shell wave function.

We do not have a relativistic treatment of the non-radiative attachment process. Thus we must try to extrapolate eqn.I.D.7 to the relativistic regime by picking the correct substitution for the β terms. I originally assumed that momentum was the correct variable here, not velocity, and used the substitution $\beta \rightarrow \beta\gamma$. This implies that the density of states must also be corrected by γ^2 . Wilson [ref.14] discusses three possible substitution schemes:

$$\beta \rightarrow \sqrt{(2E/M_n)} \quad \text{I.D.8.a}$$

$$\beta \rightarrow \sqrt{E(E+2M_n) + E - M_n}^2 \quad \text{I.D.8.b}$$

$$\beta \rightarrow \sqrt{E(E+2M_n)} / M_n \quad \text{I.D.8.c}$$

where E is the projectile kinetic energy per nucleon and M_n is the atomic mass unit. Substitution I.D.8.a is purely non-relativistic and allows $\beta > 1$. Substitution b assumes that kinetic energy is the relevant variable and was originally discussed by Raisbeck and Yiou [ref.4] as the correct extrapolation. Substitution c is the momentum extrapolation. These three substitutions differ by orders of magnitude in their predictions of the attachment cross section. We have a set of data in which non-radiative attachment is the dominant process and will determine which is the best extrapolation to use.

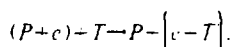
Jackson and Schiff [ref.16] also attacked the problem of non-relativistic non-radiative electron attachment and included the interaction between the projectile and the target nucleus in their perturbation calculation. The role of this part of the Hamiltonian in an exact calculation is not clear [ref.16], especially at high velocities. Their calculation is done for protons on hydrogen and is not easily generalized to more complicated systems. Mittleman has made a relativistic calculation for $p-H$ systems [ref.17]. Again this calculation is not readily generalizable to more complicated systems. A discussion of these points is presented in the work by McDowell and Coleman [ref.18] which views these approaches.

I.D.1.c. Capture into excited states

Extensions of these calculations to account for single electron capture into excited states of the projectile were originally discussed by Oppenheimer [ref.12]. He calculated transition probabilities for arbitrary eigenstates (n,l,m) of the projectile and found that cross sections for capture into states for which $l,m \neq 0$ fall off more rapidly by $(\alpha/\beta)^2$ than for capture into $n,0,0$ states. He approximated the capture cross section at high β into state $n,0,0$ as $\sigma_n = \frac{1}{n^3} \sigma_1$. To account for capture into excited states of the projectile we need only sum over n . Since $\sum_n 1/n^3 = 1.202$, we may account for capture into all excited states by multiplying eqn.I.D.5 or I.D.7 by 1.202.

I.D.2. Electron Stripping

The process of electron loss can be represented schematically as



where P is the bare projectile nucleus, e is the electron to be stripped from the projectile ion and T is the target. The dashed parenthesis indicates that the stripped electron may become attached to the target atom or may become free. The prime on T in the final state represents the fact that a target atom may be left in an excited state.

In one subset of final states the electron is transferred to a bound state in the target atom. This process is charge exchange with the target atom, i.e. the same process discussed above as non-radiative capture with the role of projectile and target reversed. This process contributes a negligible amount to the stripping cross section at the energies involved in this experiment because our attachment cross section is always much smaller than the stripping cross section.

In all other final states the projectile ion has suffered an ionizing collision with some effective target and the electron has become free. The effective target in any individual collision may be taken for calculation to be an electron, a nucleus or an atom from the medium. A

calculation of the cross section for this process implies integrating over all final states of the target and projectile for interactions in which the energy transfer to the projectile's electron exceeds the electron's binding energy.

There is no exact solution for the problem of single electron stripping by complex targets. To obtain an estimate of the stripping cross section we first go to the reference frame in which the projectile ion is at rest. In this frame the target atom passes the ion at speed β and liberates the ion's electron in an ionizing collision.

An intuitive basis for understanding the magnitude of the stripping cross section for simple ionizing collisions comes from Bohr [ref.19]. He presents a semi-classical calculation done in the free collision approximation, which is valid only if the incident velocity is greater than the orbital velocity of the stripped electron. He obtains the stripping cross section, σ_s , by integrating the Rutherford cross section over all energy transfers greater than the binding energy of the electron in the hydrogenic ion, assuming the energy transfer spectrum is the same for bound electrons as for free electrons.

Bohr suggests two limiting forms for the loss cross section depending on whether the electrons and nuclei of the target medium can be treated as independent scattering centers or must be treated together as a collective scattering potential. In small impact parameter collisions the nucleus and electrons of the target atom act as independent scattering centers. In this classical picture, the energy transfer to the bound electron, δE , as a function of impact parameter, b , can be written as $\delta E = 2\alpha^4 a_0^2 m_e Z_T^2 / \beta^2 b^2$. The ionization potential for the ground state of the projectile can be written as $I = \alpha^2 m_e Z_P^2 / 2$. Thus for $b > 2\alpha a_0 Z_T / Z_P \beta$ no ionization can take place.

We can calculate the cross section in this independent scatterer approximation as long as the impact parameter corresponding to an energy transfer greater than the ionization potential is smaller than the orbital dimensions of the target atom, i.e. for $\frac{\alpha Z_T^2}{\beta Z_P} < 1$. If this condition is not fulfilled we can no longer treat the electrons and nucleus as independent and must consider

scattering from a screened nuclear potential as a more valid approximation. We will present data for high atomic number targets which require use of a screened potential to calculate the stripping cross section.

Bohr suggests his eqn.4.2.4¹⁹ to describe the stripping cross section per target atom in the independent scatterer approximation. This is

$$\sigma_s = 4\pi a_0^2 \left(\frac{\alpha}{Z_P \beta} \right)^2 (Z_T + Z_T^2) \quad \text{I.D.9}$$

The Z_T^2 term comes from scattering by the target nucleus while the Z_T term arises from a sum over scattering from all the electrons in the target atom.

As pointed out by Dmitriev et al. [ref.20] this equation does not correctly account for the distant collisions, i.e. large impact parameters, in the ionization process. A more realistic estimate of the ionization cross section for a fast particle of charge Ze liberating an electron from the n,l shell of a hydrogenic ion of atomic number Z_P can be obtained from sec.XVI-9 in the text by Mott and Massey.²¹ Thus

$$\sigma'_{n,l} = 4\pi a_0^2 \left(\frac{\alpha}{Z_P \beta} \right)^2 Z^2 c_{n,l} \ln \frac{2m_e \beta^2}{C_{n,l}}, \quad \text{I.D.10}$$

where

$$c_{n,l} = \frac{Z_P^3}{a_0^2 n^2} \int x_{nl,k}^2 dk,$$

$$x_{nl,k} = \int x \psi_{nl} \psi_k d^3x \text{ and}$$

$$C_{n,l} \approx 0.1 Z_P^2 \alpha^2 m_e / 2n^2$$

The constant $c_{n,l}$ is an integration over dipole matrix elements $x_{nl,k}$ connecting the wave function of an electron in the n,l shell to the wave function of a free electron of momentum k . The constants c_{nl} and C_{nl} were originally computed by Bethe [ref.22] for hydrogen ions.

Equation 1.D.10 must be modified for relativistic effects before it can be used to calculate cross sections for our data. Wilson [ref.7] used Mott and Massey's relativistic ionization cross section (ch.XXII-2 [ref.21]) to arrive at the following stripping cross section, still in the independent scatterer approximation:

$$\sigma_s = 4\pi a_0^2 \left(\frac{\alpha}{Z_p \beta} \right)^2 (Z_T^2 + Z_T) C_1 \left(\ln \frac{(4\beta^2 \gamma^2)}{(C_2 \alpha^2 Z_p^2)} - \beta^2 \right), \quad 1.D.11$$

where $C_1 = 0.285$ and $C_2 = 0.048$. These values for C_{II} and C_{III} were computed by Bethe for ionization of the K-shell electron of a hydrogenic ion. This equation is familiar from studies of energy loss where the stripping of electrons of the medium accounts for the portion of the energy lost to ionization by a fast charged particle traversing matter. The Z_T term in eqn.1.D.11 again arises from a sum over the contributions from all individual electrons in the target atom while the Z_T^2 term accounts for the ionization by the nuclei.

Mott and Massey discuss the changes to the ionization cross section formula resulting from scattering of electrons by electrons. They conclude that the formula used in 1.D.11 based on scattering by heavy particles should be good to $\approx 10\%$ for scattering by electrons in the relativistic regime (ch.XXII-2 [ref.21]). Wilson [ref.7] notes that equation 1.D.11 reduces in the non-relativistic limit to the equation presented by Dmitriev et al. [ref.20] for atom-atom collisions. Fowler et al. gave a similar equation for the stripping cross section [ref.23]. Equation 1.D.11 will be shown to provide a much better fit to our data than does the Bohr formula, eqn.1.D.9.

Bohr presents his eqn.4.2.8 to describe cases where screening effects become important. This will be the case for heavy media such as the Ag and Au targets used in this experiment.

$$\sigma_s = \pi a_0^2 \frac{Z_T^{2/3}}{Z_p} \left(\frac{\alpha}{\beta} \right) \quad 1.D.12$$

We will find that this formula provides a reasonable fit to our high Z_T data.

As mentioned above, the stripping cross sections measured here may contain contributions from all eigenstates of the hydrogenic ion since the lifetimes of excited states may be long compared to the mean time between collisions. The relatively long lifetimes introduce a complication in computing the stripping cross section since multiple collision ionization processes may be important. Calculation of the stripping cross section involving multiple hit processes are complicated and will not be further discussed. We note that calculations involving only single hit processes may underestimate the cross section but the effect should be smaller than the uncertainties associated with our measurements.

I.E.Scope of data presented

The scope of data available from this experiment is summarized in Table 1. To provide a broad data base for comparison with theory we have performed measurements of σ_a and σ_s for C, Ne and Ar ions covering the energy range from 140 to 2100 MeV/nucleon ($0.5 < \beta < 0.95$). We studied nine separate beam/energy combinations, each of which constituted a separate run. The targets were foils composed of selected elements from Be to Au. We also studied composite target systems consisting of Mylar films. The data thus cover both the radiative and non-radiative regions of electron attachment and the independent scatterer and screened potential regions for stripping.

The number of different foil thicknesses available for each target species varied from a single thickness for Ni($Z=28$) to as many as 6 separate thicknesses for Al($Z=13$). Thus for some target elements we were able to determine only the equilibrium ratio, R_{eq} , while for most we could determine σ_a and σ_s individually.

Previous experiments involved projectiles of either lower atomic numbers or lower velocities so that our data set is unique. We make comparisons to other data only through extrapolations from theoretical formulations that fit our data set.

We compare our measured electron attachment cross sections to predictions based on equations I.D.5 and I.D.7 by isolating regions in which either the radiative attachment or the

non-radiative attachment process dominates. In the region of the independent scatterer approximation, we compare our measured stripping cross sections to both eqn.I.D.9 and I.D.11. We compare data from the region in which screening is important to equation I.D.12

EXPERIMENTAL DETAILS

II.A.Introduction

A diagram of the experimental set-up is shown in Fig.1. A diagram of the experimental electronics is shown in Fig.2. Beams of fully stripped ions from the Bevalac were transported down Channel II to a focus (F3) at the target area. We inserted targets consisting of free standing foils at the focus F3. The spectrometer system immediately downstream of the target was tuned to focus the beam of hydrogenic ions emerging from the target onto a detector telescope approximately 18 m downstream of the target location. The number of fully stripped ions emerging from the target, N_0 , was obtained from a secondary emission monitor (Sec.II.E). The number of single electron ions, N_1 , was counted by the detector telescope (Sec.II.F). Data from the various counters and telescope were collected on a computer controlled (PDP 11/45) data collection system. Final analysis was performed at the LBL CDC 7600 computer facility.

For some of the experimental runs an independent data collection system consisting of single scintillator detectors connected to scaler readouts was used as a backup check of the more complicated computer controlled apparatus. A diagram of the electronics for this back-up experiment is shown in Fig.3.

In the remainder of this section each of these items will be described in detail.

II.B.Bevalac

The Super-Hilac-Bevatron accelerator providing beams for this experiment is described in [ref.24]. The Hilac provides beams of fully stripped nuclei at 8.5 MeV/nucleon which are injected into the Bevatron. The Bevatron accelerates these nuclei to kinetic energies as high as 2600 MeV/nucleon.

The Bevalac is a pulsed accelerator that delivers beam at a rate from 10 to 15 pulses per minute, depending on the extraction energy. Particle fluxes ranged from 10^4 to 10^9 particles per pulse during the course of the experiment, although at any data point (i.e.

beam/energy/target combination) fluxes were held constant to $\approx 25\%$. Typical measurement times varied from 10 minutes to one hour per data point.

To eliminate charge exchange effects in the transport system, the beam channel was sealed and pumped to a pressure of $< 10^{-6}$ torr. Two bending magnets (X2M5 and X2M7) and a set of vertical and horizontal jaw collimators restricted variations in the rigidity ($=\beta\gamma M/Ze$) of particles delivered to the target to $< 0.1\%$.

II.C.Targets

The target species used in this experiment are listed in Table 1. Parameters of the actual targets are given in Appendix 1. Targets were typically 8 cm. in diameter and ranged in thickness from $\approx 50 \mu\text{g}/\text{cm}^2$ to a few mg/cm^2 . Each target was supported on an aluminum frame which had an 8 cm. hole in the center over which the foil was stretched. Targets were inserted in the beam singly or in combinations (to increase the choice of effective thicknesses). We also had an empty target holder available for each run which was periodically inserted during measurements of background. Signals from this empty frame constituted the "target out" correction.

The targets contained a set of standard targets used in every run, to assure consistency, and a set chosen specifically for each beam-energy combination. The standard set was chosen to provide equilibrium ratios covering a broad range in target charge. The specific sets were chosen to provide the most information on σ_a and σ_s , within the constraint of available beam time. Predictions for these targets were based on the equations presented by Raisbeck and Yiou [ref.4]. Thicknesses were selected, where possible, to bracket the predicted equilibrium thickness, thus providing a good data set to fit the growth curve.

Many of the targets were procured as thin foils while others were fabricated by standard evaporation techniques at LBL. An examination of the form of the growth curve (eqn.I.C.6) indicates the importance of determining the target thicknesses accurately to obtain values of σ_a and σ_s . To determine values for equilibrium ratios, however, it is sufficient to know that

targets are thicker than the equilibrium thickness (defined here as the thickness leading to a value $N_T/N_0 = 0.9 R^{-1}$).

There are actually two separate problems associated with measurement of target thickness: determination of absolute thickness and determination of thickness uniformity. Absolute thicknesses were determined by weighing samples of accurately known area. The chemical composition of the target foils was well known but the matter density was not: from the weight of a known area of foil we can determine the number of target atoms per cm^2 directly. For purposes of calculation, especially in the growth curve, we use the target thickness in units of number of atoms per cm^2 .

To determine uniformity, energy loss by collimated (0.5mm), monoenergetic alpha particles was measured at a number of positions across the face of each foil. This method could in principle also yield absolute thickness. However, uncertainties in the range energy relation for low energy alpha particles introduced significant uncertainty in thickness values obtained in this way. The thickness variations in the least uniform foil were less than $\approx 10\%$.

II.D.Spectrometer

The Bevalac Beam-33 spectrometer [ref.25] was used to focus the hydrogenic ion beam emerging from the target and separate it spatially from the fully stripped beam. The acceptance of this spectrometer system is $\pm 12.5 mrad$ which is much larger than the beam divergence ($< 2 mrad$), multiple scattering in the target ($< 10 \mu rad$) and angular distributions resulting from momentum transfer in the capture and loss processes ($< 10 \mu rad$) combined. Thus there are no corrections for spectrometer acceptance.

The bending magnet of the spectrometer was set to bend the fully stripped beam thru 12° (see Fig.1) placing it at a rail distance of $D_0=200cm$. (The magnet current required to accomplish this together with the calibration values for the magnet provides a measure of the beam energy.) Ions passing through the bending magnet field with an electron attached are bent through a smaller angle because of their higher rigidity and emerge at a rail location

$D_1 = ((Z_p - 1)/Z_p) D_0$. Typical separations between single-electron and fully stripped ion beams ranged from 10 to 35 cm.

The spectrometer is set to focus particles of rigidity $R = Z_p R_p / (Z_p - 1)$, where R_p is the rigidity of the fully stripped beam. This setting focuses all hydrogenic ions to the position D_1 . The fully stripped ions, being a lower rigidity, are slightly defocused at the position D_0 but the beam profile spot is still small enough to lie within the solid angle viewed by the beam monitor (see section II.E).

The spectrometer volume is directly connected to the transport channel; thus it is also pumped to a pressure of $< 10^{-6}$ torr. This pressure is low enough to prevent contamination of the N_1 signal by electron attachment and stripping from the residual air. (This point was verified by increasing pressure until a change in the N_1 signal was observed. The pressure necessary exceeded 10^{-4} torr).

The detector system acceptance was larger than the focused beam spot size. Thus all hydrogenic ions delivered by the spectrometer entered the detector telescope (see section II.F for a description of the detector). This was checked experimentally by moving the detector along the spectrometer rail and mapping the actual size of the spot formed by the beam of hydrogenic ions.

The size of the spot focused by the spectrometer reflects the size of the spot at the first focus out of the Bevatron (F_1). This spot size is generally energy dependent. To assure that the spot size was constant over the course of this experiment, a collimator (1 cm) was placed at F_1 in all runs.

The beam position at the entrance of the spectrometer, F3, and at the spectrometer rail, is sensitive to currents in the upstream bending magnets. To insure stability of these positions a beam steering system consisting of position sensitive scintillators in a magnet current feedback loop was used. The scintillators were periodically placed in the beam to check actual beam position. If the position was not correct, the magnet currents were altered accordingly. These currents were recorded for every beam pulse and any data taken during a pulse that had

incorrect currents was discarded. This occurred for $<10^{-4}$ of all beam pulses.

II.E. Beam monitor

The ratios N_1/N_0 expected in this experiment were as low as 10^{-9} ; thus 10^9 beam particles had to be counted for each hydrogenic ion formed. Beam time limitations required operating at the highest beam intensities available. This made it impossible to perform beam control and monitor functions with single-particle counting devices. For beam steering and intermediate flux monitoring a current-mode scintillator array was used. To determine beam fluence N_0 , a secondary emission monitor (SEM) was used.

The current mode device used for beam steering consisted of a thin scintillator viewed by a photomultiplier whose anode was connected to a current monitoring circuit [ref.26]. The current output of the photomultiplier tube integrated over a beam pulse was proportional to the number of particles that passed through the scintillator.

Current-mode scintillators were used in the beam steering circuit to maintain beam position on the target and at the spectrometer rail. Two scintillators at the target were periodically placed in the beam to check left-right asymmetry which would result from drifts in the current in the X2M7 magnet. Four scintillators behind the rail (Fig.1) continuously monitored left-right and up-down asymmetries to check stability of M1M2 and X2M5S currents. These currents very rarely changed in the course of a run. In addition, a large current-mode scintillator centered on the beam at the rail provided a cross-check of the beam fluence recorded by the SEM scintillator telescope.

The secondary emission monitor (SEM) used to determine beam fluence N_0 consisted of a three element scintillator telescope viewing a thin Pb plate. The individual scintillators were 2.5cm., 10cm. and 20cm. squares arranged as shown in Fig.1. The Pb plate was placed in the beam path at an angle of 45° . Beam induced interactions in this Pb plate led to the emission of energetic protons and assorted other charged particles, a small fraction of which penetrated the SEM scintillators. Uninteracted beam proceeded through the experimental cave area into a re-

entrant well beam stop 5m downstream of the counters. The scintillators were run in coincidence pairs, i.e. 1+2 or 1+3, to diminish background contamination and provide well defined geometrical acceptance. Scintillator threshold and coincidence levels were set for each beam to optimize the scaling factor with respect to the N_1 rate, the SEM count rate and the beam flux.

Calibration of this SEM system implies measuring the efficiency, η_{SEM} , of the secondary emission monitor for counting individual beam ions. Beam rates low enough to count on a particle-by-particle basis in a single scintillator (called RTOT) were used to measure this efficiency. Then $\eta_{SEM} = N_{SEM}/N_{RTOT}$, where N_{SEM} is the number of counts recorded by the SEM while RTOT recorded the passage of N_{RTOT} fully stripped ions.

RTOT was in the beam only during calibration of the SEM. RTOT was located 3 m upstream of the SEM and was outside of the geometrical acceptance solid angle for any SEM combination. Thus secondaries generated in RTOT would not be counted by the SEM. To check this and possible energy loss effects a third counter located far from the RTOT and SEM counters was used. The third counter was thus insensitive to whether RTOT was in or out of the beam.

II.F.Signal monitor

The hydrogenic ions were counted individually by a solid state detector telescope consisting of four Si(Li) detectors each 3mm thick and 44mm in diameter [ref.27]. At the velocities used in this experiment, incident ions have ranges much greater than the total thickness of the detector telescope. The detector telescope was positioned at D_1 on the spectrometer rail. The area of the detectors was \approx four times the area of the beam spot. A measurement of the beam spot size in each run indicated that $<3\%$ of the single electron ions missed the detector telescope. Figure 1 shows the detector telescope layout and a sample signal spot size.

The equilibrium ratios measured in this experiment are all $<10^{-4}$ indicating that the ions spend most of their path length in matter in a fully stripped state. Signals generated in the detectors are proportional to $dE/(dX=F \cdot Z \cdot B)$. The signal from each detector is sent to a

separate charge sensitive pre-amplifier ($1\mu\text{sec}$ time constant, see Fig.2). Each pre-amp is connected to a separate 12 bit dual gain ADC having a dynamic range of 4×10^4 .

The detector telescope was calibrated for each beam by placing it in the direct low intensity beam and recording a number of beam particle events. This gave a pulse height distribution such as is shown in Figure 4. A maximum likelihood method based on these distributions was used to determine the nuclear charge of each recorded event.²⁸

The first two detectors in the telescope (D_1 and D_2) each had a fast discriminator on their pre-amp signals. Thresholds on these discriminators were set at levels corresponding to a signal from a beam velocity nucleus of atomic number Z_p-2 . An event trigger was defined as a coincidence between the discriminator outputs of these two detectors ($D_1.D_2$) when the data collection system was "live". (See Sec.II.G. for a discussion of "live" time.)

To allow us to insure that the particle generating an event trigger passed through the active area of the detectors, a circular scintillator slightly smaller than the detector diameter was placed directly in front of the detector telescope. The anode signal from the photomultiplier tube viewing this scintillator was passed through a discriminator whose threshold was set near the level expected from a beam velocity nucleus of atomic number Z_p-4 . A logic pulse (called the "in-geometry" pulse) was generated each time this discriminator fired in coincidence with $D_1.D_2$.

A second pulse was generated when this discriminator fired during the process of analog-to-digital conversion in the ADC chain. This pulse (called the "pile-up" pulse) allowed us to determine whether a second particle entered the detector telescope during data conversion. The beam intensity was kept well below the rate at which significant pile-up occurred.

II.G.Data collection

Data collection and control functions were performed by a PDP 11/45 minicomputer. The computer performs three basic tasks: data collection, beam line and detector control, and on-line data analysis. Bevatron internal timing signals were used to switch CPU attention among these three functions.

The most important of the three functions is data collection. On arrival at the CPU of the "flat-top on" signal, which is generated when the main magnetic field of the Bevatron reaches the level required to extract the specified beam energy, the data collection program "rundata" takes control of the 11/45 CPU. This program is responsible for reading, through a CAMAC²⁹ interface, all of the devices associated with each event. These consist of the detector ADC's, "live-time" scalars controlled by the detector telescope and the "ir.-geometry" and "pile-up" pulses. At the arrival of the "flat-top end" signal, generated 100msec. after the end of particle extraction from the Bevatron, all monitor scalars are read. These include the SEM, current mode, neutron monitor and single particle scalars. After reading these scalars, control of the CPU is turned over to background analysis programs.

At the middle of each "flat-top" a special program temporarily halts data taking and inquires the status of all control devices. Control devices include magnet current monitors and controllers, beam steering scalars and detector position encoders. All control data are checked to make sure no device is operating outside predetermined limits. Necessary corrections are made automatically. Data taken during periods when any control device was outside its limits were discarded. This occurred for <1% of the data.

In background analysis time the computer sorts data taken during the preceding "flat-tops" and performs simple calculations on these data. Such calculations include keeping running sums of all scalars and integrity bits, calculating the most probable nuclear charge for each particle producing an event and forming histograms and scatter plots of various parameters. These calculations are fed to display routines that allow the operator to keep watch over the progress of the experiment.

Data were accumulated by a double buffering method using three levels of storage: core memory, magnetic disc and magnetic tape. Data from the most recent event were stored in core memory buffer A. When buffer A became full, data from the next event would start to fill buffer B and buffer A was read out onto a magnetic disc. Similarly, when buffer B became full, data would be routed to buffer A while B was read onto disc. When a disc reached its capacity to store data the collection process was halted and data transferred to a magnetic tape. Disc capacity was $\approx 30K$ events. This procedure minimized computer-related dead time in the data taking process. Data tapes were then taken to the LBL CDC 7600 system for final analysis.

An important feature of this collection system was that, whenever an event trigger was accepted, the CPU issued a signal to halt all data collection functions. Generation of further event triggers was inhibited until that event was read and a computer clear signal was issued (typically $200 \mu \text{ sec.}$). In particular, the many scalers that were recording beam fluence information were prevented from counting beam particles during the time when event triggers could not be generated. This procedure made it possible to interpret the data without the necessity for making "dead time" corrections.

II.H.Backup experiment

For the low energy C and Ne runs a completely separate detector system was run in parallel with the computer controlled detector telescopes. A two scintillator "telescope" was placed in front of the detector telescope at D_1 . This backup experiment was motivated by its simplicity and the comparative complexity of the data collection system described previously. However, this simple system could be used only at the low energies where the signal rate at D_1 from hydrogenic ions was much greater than the rate from competing background signals. Data from this backup experiment served as a very useful check on the integrity of data from the complete system.

The scintillator photomultiplier tube signals were fed to separate discriminators whose thresholds were set at the levels expected from beam-velocity nuclei of atomic number Z_p-2 .

just as the detector telescope thresholds were set. The discriminator outputs were fed through a coincidence circuit to generate a gate for a pulse height analyzer. The pulse height distribution from one of the scintillators was recorded. The number of particles of each atomic number was determined from the total in each peak. Projectile fragmentation in the target and upstream matter accounted for the appearance of peaks at other than the atomic number of the beam. The number of single electron ions was obtained by integrating the peak corresponding to the atomic number of the beam. The total number of beam particles for each run in this backup experiment was determined from the ungated scaler recording SEM counts.

ANALYSIS

III.A. Introduction

In this section we discuss the analysis used to extract the equilibrium ratio, R_{eq} , or the attachment and stripping cross sections, σ_a and σ_s , from the measured quantities N_0 , N_1 and target thickness, x . The number of incident beam particles, N_0 , is determined from the beam monitor and its calibration (Sec.III.B). The number of emerging single electron ions, N_1 , is determined from the counts in the signal monitor (Sec.III.C). Both N_0 and N_1 were suitably corrected for background (Sec.III.D). From these values the ratio N_1/N_0 was determined for each beam/energy/target combination. The value of x , the target thickness, was measured as described in section II.C.

The ratio measurements for sets of target species/thickness divide naturally into three groups. In the first group the ratio was measured for only one target thickness of a given species. In this first group we always chose a thick target so the R_{eq} value was determined directly. No determination of the individual σ_a or σ_s values could be made for these target species without recourse to systematics determined from the remainder of the experimental data. In the second group are target species/thickness sets consisting of measurements for two separate target thicknesses for the same beam/energy combination. We could determine σ_a and σ_s from measurement for only two thicknesses when one of the targets was thinner than the equilibrium thickness, T_{eq} , and the other was $\approx T_{eq}$. In the third group are target species with multiple target thicknesses for the same run. These form the most useful data set: a fit to the growth curve yields values for σ_a and σ_s even in the presence of fluctuations in any single measurement. The determination of the confidence intervals associated with each of these fitting parameters was explored in detail because of the statistical correlation between the parameters.

The energy dependence in the theoretical formulations of the cross sections required that the beam energy be determined as accurately as possible.

Each of these points is discussed in detail in the following sub-sections.

III.B. Beam fluence, N_0

The total number of incident beam particles was obtained from the beam monitor described in Sec.II.E.2. The efficiency of this monitor, η_{SEM} , was re-calibrated periodically throughout each run using single particle counter RTOT, but was not checked for each data point. At each calibration, the beam to monitor ratio was determined to a statistical accuracy of better than 3%. However, the variation in this ratio was considerably larger, typically 7% to 10% over the course of a full run. These variations were attributed to fluctuations in the gain of the photomultiplier tubes viewing SEM and RTOT scintillators and to drifts in discriminator thresholds such as would be expected from temperature changes and drifts in applied tube voltage. No attempt was made to lessen these effects and an overall uncertainty in beam fluence of 10% is assigned.

The mean value of the monitor efficiency is determined as the simple arithmetic mean of all the calibration points taken during a run. The variance in this ratio is taken as the square root of the sum of the squares of the deviations from the mean divided by the (number of observations - 1). The value of N_0 is then determined for each data point as the number of monitor counts, N_{SEM} , divided by this efficiency factor; i.e.

$$N_0 = N_{SEM} / \eta_{SEM} \quad \text{III.B.1}$$

The uncertainty in N_0 is then obtained by adding in quadrature the statistical uncertainty in N_{SEM} and the uncertainty from η_{SEM} .

III.C. Single Electron Ions, N_1

The number of single electron or hydrogenic ions formed in each run, N_1 , is determined from the number of events recorded by the detector telescope as having a charge equal to the nuclear charge of the beam, N_{ev} . This number is determined by the maximum likelihood method applied to all events recorded by the detector telescope. N_{ev} is corrected for geometrical losses and for fragmentation losses in the detectors, vacuum tank window and target. In the low energy runs for C and Ne ions an additional correction for the presence of the backup experiment scintillators was also made.

Approximately 8% to 10% of the ions striking the front detector of the telescope suffer a fragmentation reaction within the telescope. The signal from such a fragmented ion is not a clear signature of its initial charge upon entering the telescope. These events are removed from the data in a likelihood analysis of the signals from all four detectors. This leads to a correction of typically 2–3% per detector and can be accounted for by the fragmentation cross section in Si.

Nuclear fragmentation reactions within the vacuum window and target yield a negligible correction since they are typically $<10 \text{ mg/cm}^2$ thick. However, the scintillators of the backup experiment (Sec.II.H) lead to an additional correction of 2–3% for some of the runs.

The number of hydrogenic ions formed in the target is given by

$$N_1 = N_{ev} / \eta_B \quad \text{III.C.1}$$

where η_B is the appropriate correction for that beam. This factor includes corrections for data discarded in the likelihood cuts and a geometrical factor for events missing the detector telescope. Values for η_B for each run are listed in Appendix 1. Uncertainty in N_1 includes statistical uncertainty in N_{ev} and uncertainty from the correction factor η_B .

III.D. Background

No background corrections to either N_0 or N_1 were necessary.

Possible sources of background in N_0 would come from beam-off radiation in the experimental cave area or from singles contamination to the coincidence rate. Thresholds on the SEM scintillators were set much higher than the signal from a singly charged particle having sufficient energy to penetrate two scintillators. Thresholds on these scintillators were set so that beam-off count rates were zero over times long with respect to any data collection time. Singles rates were constantly compared to coincidence rates. When the singles contamination from one pair of SEM scintillators got above 1%, a different, smaller geometry, pair was used.

Background in N_1 signal could come from electron pickup in the residual air of the spectrometer system or from fragmentation products generated in the target or elsewhere. Target out checks were made for each data point. The number of N_1 counts in target out runs were null for beam fluences which would have resulted in generation of 100 events with target in.

No beam charge fragments generated in the target would appear at $D_1 \pm \delta D_1$ since this would require multi-nucleon pickup and a large increase in the ion's momentum in an interaction within the target; (δD_1 is the detector radius, 2.5 cm.). Beam charge fragments generated in the spectrometer window material would show up in target out runs. Contamination from other charged particles generating signals in all four detectors of the detector telescope is expected to be $<1\%$ since the charge resolution of the individual detectors is ≈ 1 charge unit. Thus no background corrections to either N_0 or N_1 were necessary.

III.E. The ratio $R = N_1/N_0$

The ratio of hydrogenic ions to fully stripped ions was determined for each beam/energy/target/thickness combination from the corrected number $N_1 = N_c/\eta_B$ and the scaled number $N_0 = N_{SEM}/\eta_{SEM}$ (see sections III.B and C). Thus $R = N_1/N_0$. Uncertainty in this ratio was computed by adding in quadrature the uncertainty in N_1 and N_0 . Typical uncertainties in this measured ratio were from 12% to 20% with some as large 30%. These values are listed

for each measured data point in Appendix 1.

III.F.Targets

As seen in section III.H, target thickness determination is critical only in determining σ_a and σ_1 , not for determining equilibrium ratios. Target thickness determinations were discussed in section II.C. Typical uncertainties in target thickness as listed in App.I were <10%. The number of different thicknesses used for each species of target varied from one to nine.

The only target requiring special discussion is the Mylar target. We report our cross sections for attachment and stripping per target molecule assuming that the composition of Mylar is $C_5H_4O_2$. To calculate cross sections for comparison with our measurements we simply sum over the contributions from each of the elements comprising the molecule.

III.G. Determination of R_{eq}

For thick targets, i.e. when $x > \sigma_s^{-1}$, where x is measured in number of atoms per cm^2 , the ratio of single electron ions to fully stripped ions approaches a limiting value called the equilibrium ratio. This ratio can be determined from a measurement of N_1/N_0 for a single target provided that target is sufficiently thick. For some species of targets a determination of N_1/N_0 was made only for a single thickness. Thus, as seen in Tables 3-5, some targets have only R_{eq} values reported. To insure that these data were taken for sufficiently thick targets we used the systematics determined for the whole data set to make predictions of the thickness required to reach equilibrium. This thickness is defined somewhat arbitrarily as the thickness at which a measurement of R would yield a value of $0.9R_{eq}$. These thicknesses are also listed in Table 3.

III.H. Determination of σ_a and σ_s

Values of the single electron attachment cross section per target atom, σ_a , and the effective stripping cross section per target atom, σ_s , are obtained from the measured ratios and target thicknesses by fitting to a simple growth curve. The derivation of this curve and its applicability to this data are discussed in section i.C. A typical fit to the growth curve is shown in Fig.5 for 400 Mev/nucleon Ar on Mylar.

The growth curve provides an estimator for the mean value of the ratio $R=N_1/N_0$ as a function of target thickness. Thus

$$\bar{R}_i = \frac{\sigma_a}{\sigma_s} (1 - e^{-\sigma_s x_i}) , \quad \text{III.H.1}$$

where \bar{R}_i is the predicted mean value for the ratio expected from a target whose thickness is x_i (in atoms / cm^2). We find the most probable values for the parameters σ_a and σ_s by minimizing the statistic;

$$f(\sigma_a, \sigma_s) = \sum_i (R_i - \bar{R}_i)^2 / \delta_i^2 , \quad \text{III.H.2}$$

where i signifies a target of thickness x_i , R_i is the ratio measured for that target, \bar{R}_i is the value predicted by eqn.III.H.1 and δ_i is the uncertainty in the difference $R - \bar{R}$. The factor δ contains terms from the statistical uncertainty in the measured value, R_i , and from uncertainty in the estimator, \bar{R}_i , resulting from uncertainty in the measured target thickness, δx_i . Thus:

$$\delta_i = \sqrt{\delta R_i^2 + (\sigma_a e^{-\sigma_s x_i} \delta x_i)^2} . \quad \text{III.H.3}$$

A first guess at σ_a can be obtained from R_i/x_i , where i represents the thinnest target in the set. A first guess at the value for R_{eq} can be obtained from the measured R for the thickest target in a set.

Assignment of uncertainties to the two fitting parameters, σ_a and σ_s , is complicated by the fact that f is not simply chisquare distributed. This means that errors determined through

the covariance matrix, the method employed in most minimization routines, will not necessarily reflect the standard confidence level. A correct method for determining these uncertainties is to determine the value of f corresponding to e.g. a 68% confidence level, $f_{0.68}$, and then vary σ_a and σ_s separately (holding the other one fixed at the most probable value) until the value of f for the data set is equal to $f_{0.68}$. This analysis indicated that standard error assignments were nearly equal to the correct values. The standard errors determined by the minimizing routine STEPIT [ref.30] are reported.

III.J. Confidence levels

We checked the interpretation of the error assignments by a Monte Carlo method in which we generated data sets from the measured ratios and target thicknesses, fit these data to the growth curve and examined the resulting distributions of σ_a and σ_s values. To do this, we first selected a data set (e.g. the six measurements for 400 Mev/nucleon Ar on Mylar). R and x_i values are assumed to be drawn from normal distributions with standard deviations given by the uncertainties quoted in App.1. For each data point in the set, we first pick a target thickness from the normal distribution whose mean is the measured target thickness and whose standard deviation is the quoted uncertainty in thickness; i.e. we pick x_i' from $N(x_i, \delta x_i)$. We then predict the expected ratio for this target thickness using the best values of σ_a and σ_s obtained from the actual data set; i.e. $\bar{R} = \sigma_a / \sigma_s (1 - e^{-\sigma_s x_i'})$. We then pick a random value for R_i' from the normal distribution whose mean is \bar{R}_i' and whose standard deviation is the quoted uncertainty in the actual measured ratio. We repeat this once for each measured thickness to generate a simulated data set equivalent to the measured data set. This simulated set is then used as input to the fitting routine and values of σ_a' and σ_s' are determined.

Based on a Monte Carlo simulation of 1000 data sets for our selected beam-target combination (Ar^{40} on Mylar at 400 Mev/nucleon), we find that the statistic (III.H.2) is distributed as shown in Fig. 6. The experimental distribution of this statistic has a mean of 0.5 and width of 0.4, suggesting that the quoted uncertainties in our measured ratios and target thicknesses may

be somewhat large.

The distribution of values for σ_a' , σ_s and R_{eq}' ($=\sigma_a'/\sigma_s$) from the fits to these 1000 data sets are shown in Figs.7a,b and c. The widths and asymmetries of these distributions can be compared to the widths represented by the uncertainties in the parameters σ_a and σ_s as assigned by the procedure discussed in sec.III.H. This comparison shows that the quoted uncertainties represent fairly the Monte Carlo distributions.

III.K. Beam Energy

The beam energy in each run was determined to an accuracy of $\approx 1\%$ by a combination of three separate procedures. The first method was applicable in all runs and is based on the fact that the Bevalac is a synchrotron. Thus the energy of the extracted beam can be estimated from the magnetic field and extraction radius of the machine. This value must be corrected for energy loss in the $\approx 1 \text{ gm/cm}^2$ of material in the channel at the first external focus. The second method relies on the calibration of the Beam-33 spectrometer magnet. From the magnet current required to bend the fully stripped ion beam through 12° and the calibration of this magnet we could determine incident ion energies to $\approx 1\%$. The final check was possible only for the 140 MeV/nucleon and 250 MeV/nucleon beams and relied on the range-energy relation for a precise thickness of copper absorber. When all three methods were employed agreement was obtained at the 1% level. Note that energy loss in the targets is completely negligible.

RESULTS and DISCUSSION

IV.A.Introduction

The scope of data available from this experiment is shown in Table 1. The raw data are presented in Appendix 1. Values of the equilibrium ratios are presented in Table 3 and discussed in Sec.IV.B. Values of the attachment cross sections, σ_a , are given in Table 4 and discussed in Sec.IV.C. Values of the stripping cross sections, σ_s , are given in Table 5 and discussed in Sec.IV.D.

IV.B.Equilibrium ratios

As discussed in Sec.I.C, the ratio of hydrogenic to fully stripped ions, ($R=N_1/N_0$), becomes independent of target thickness for sufficiently thick targets and approaches a limiting value called the equilibrium ratio, $R_{eq}=\sigma_a/\sigma_s$. Measured values of R_{eq} are given in Table 3. We also list our best predictions of these ratios and indicate which attachment and stripping formulations were used for these calculations. Equilibrium thicknesses obtained from the relation $T_{eq}=2.3/\sigma_s$, are also given, where σ_s is calculated from the theoretical formulation indicated.

Predictions of equilibrium ratios and equilibrium thicknesses depend on the theoretical formulations for σ_a and σ_s , which are discussed in sec. IV.C and IV.D respectively. In Fig.8 we show a comparison between our best predictions of σ_a/σ_s and our measured values of the equilibrium ratio. From this figure we can see that we are able to calculate equilibrium ratio values for light targets (Be-Al) to within a factor of two but that for the heavier targets our calculations are in disagreement with the data by up to factors of four. We attribute most of these discrepancies to our inability to predict stripping cross sections in the region where $\alpha Z_T^2/\beta Z_P$ is near 1 (see sec.II.D.2).

In Fig 9 we show the dependence of R_{eq} on target atomic number for Ne projectiles at four velocities. The shape of these curves derives from the Z_T dependence of the attachment cross sections rather than the stripping cross sections. At low Z_T values the radiative process

dominates but at high Z_T the non-radiative process dominates. This figure indicates that there are optimal materials to be used as stripping foils in accelerator operations and that the effective charge of an ion may vary by more than an order of magnitude as a function of the composition of the matter through which it is moving.

We can relate our measurement of the equilibrium ratio to the mean charge of an ion traversing matter in the following manner: Electron attachment and stripping for a heavy ion traversing matter is a statistical process. Thus all possible charge states of the ion have a finite probability for occurring. If we pass a beam of ions through a target we expect the distribution of charge states in the emergent beam to have a mean value, \bar{Z}_e , that differs from the nuclear charge of the ion, Z_0 . At very high velocities, that is, velocities much larger than the K-shell electron velocity for the ion ($\approx Z\alpha c$), we expect $\bar{Z} \approx Z_0$. At lower velocities \bar{Z} may differ significantly from Z_0 .

Calculation of the charge state distribution requires knowledge of all attachment and stripping cross sections for the ion in the medium. Consequently, phenomenological functions are generally used to describe this distribution. Betz¹¹ has gathered data on charge state distributions and used the following function to calculate values for the mean or effective charge of an ion beam in matter:

$$\bar{Z} = Z_0 C (1 - e^{-\beta/aZ^n}) , \quad \text{IV.B.1}$$

where C , a and n are constants which depend on the medium. This functional form was originally suggested by Barkas [ref.32]. The formulation is motivated by a statistical model of the electron distribution in an atom [ref.31]. Other authors have found similar functions for the mean charge [ref.1].

At high velocities we expect only the fully stripped and single electron ions to constitute a significant fraction of the charge states populated. This is because the stripping cross sections are much larger than the attachment cross sections at these velocities. We can compute the average charge of an ion in a beam as

$$\bar{Z} = \frac{N_0 Z_0 + N_1 (Z_0 - 1)}{N_0 + N_1} \quad \text{IV.B.2}$$

When N_1 is much smaller than N_0 , this leads to the expression $\bar{Z} = Z_0 - \epsilon$, where $\epsilon = N_1/N_0$, i.e. for $\epsilon = R_{eq}$. We note that, since we can predict R_{eq} based on our formulae for capture and stripping, we could formulate a good expression for \bar{Z} in the high velocity case. However, we will compare our R_{eq} measurements to eqn.IV.B.1 to see how good a predictor it is.

As pointed out by Betz [ref.11], the values of C and n should depend on target charge and density although no simple form for this dependence is given. We can compute \bar{Z} using the values for these constants suggested by Barkas for emulsion, $C=1$, $a=1/125$ and $n=2/3$. With these values we find discrepancies of more than an order of magnitude in comparison with most of our data although it gives values remarkably close for a few of the measurements.

IV.C. Attachment Cross Sections

The attachment cross sections obtained in this experiment are listed in Table 4. We have also listed the predictions of eqn.IV.C.2 and IV.C.3 as the radiative and non-radiative cross sections and indicated which process is dominant for each point.

As discussed in Sec.I.D, there are two processes which contribute to the electron attachment cross section: radiative and non-radiative. These contributions sum to yield the total cross section for single electron attachment. Figure 10 shows the relative contributions of these two processes to the attachment cross section for Ne ions in Al as a function of projectile energy. Most of our data is in the regime where the radiative attachment process is dominant. However, we have measured six attachment cross sections in which the non-radiative process dominates. We are thus able to discuss which of the relativistic extrapolations of the OBK formula is best.

For comparison with the theoretical formulations for these two processes we can divide our data into three groups. In the first group we isolate the data for which the radiative process dominates by requiring that the predictions of eqn.IV.C.2 (our best predictor for radiative

attachment cross sections) be at least five times greater than predictions of eqn.IV.C.3 (our best non-radiative predictor) for the values of Z_p , Z_T and E_p belonging to each data point. In the second group we isolate data for which the non-radiative process dominates by requiring that predictions of eqn.IV.C.3 be at least twice as large as predictions of eqn.IV.C.2. This less restrictive condition was used because of the more limited data set available. In the third group are data for which neither process dominates. We first discuss comparisons with the radiative formulation.

The equation for calculating cross sections for radiative electron attachment into the 1s state of the projectile as discussed in Sec I.D.1 (eqn.I.D.5) is reproduced here for convenience.

$$\sigma_{ra} = \frac{(\gamma-1)^2}{(\beta\gamma)^2} \frac{3}{2} \alpha^4 \sigma_i Z_p^5 Z_T \frac{(\beta\gamma)^3}{(\gamma-1)^5} M(\beta) \quad \text{I.D.5}$$

$$\times (\alpha Z_p)^{2\epsilon} e^{-\frac{\alpha Z_p}{\beta} \cos^{-1}(\alpha Z_p)} \left[1 + \pi \alpha Z_p \frac{N(\beta)}{M(\beta)} \right].$$

The variables and functions in this equation are defined in sec.I.D.1. We compute a value of χ^2 for comparison between our measured radiative cross sections, $\sigma_{ra}(meas)$, and the predictions of eqn.I.D.5 as:

$$\chi^2 = \sum (\sigma_{ra}(meas) - \sigma_{ra})^2 / \delta \sigma_{ra}(meas)^2, \quad \text{IV.C.1}$$

where $\delta \sigma_{ra}(meas)$ is the error associated with measurement of σ_{ra} . The value of χ^2 per degree of freedom is ≈ 5 .

As discussed in Sec.I.C and I.D.1.c, we should obtain a better fit to our data by incorporating Oppenheimer's correction for attachment into higher states of the projectile ion. The resulting equation is

$$\sigma_{ra} = 1.202 \frac{3}{2} \alpha^4 \sigma_i Z_p^5 Z_T \frac{(\beta\gamma)^3}{(\gamma-1)^5} M(\beta) \quad \text{IV.C.2}$$

$$\times (\alpha Z_p)^{2\epsilon} e^{-\frac{\alpha Z_p}{\beta} \cos^{-1}(\alpha Z_p)} \left[1 + \pi \alpha Z_p \frac{N(\beta)}{M(\beta)} \right].$$

A value of 0.6 is obtained for χ^2 per degree of freedom by using eqn.IV.C.2 to predict values of σ_{att} used in eqn.IV.C.1. This suggests that attachment into excited states is not negligible. (We note that the first order theory based on eqn.I.D.3 gives a χ^2 of 5/DOF).

In Fig 11 we show the deviations of the data from the mean value predicted by formula IV.C.2. Here we have plotted $\sigma_{att}/\sigma_{att}^{\text{mean}}$ vs. Z_T for all data in which the radiative attachment process dominates. We see from this that eqn.IV.C.2 tends to underestimate the radiative attachment cross sections for all but the heaviest targets by $\approx 5\%$. Larger deviations for the heavy target values may result from the fact that the free electron assumption is no longer valid.

The equation for calculating cross sections for the non-radiative process based on the Oppenheimer-Brinkman-Kramers (OBK) approximation is discussed in Sec.I.D.1.b. We have culled a data set in which this process is dominant in order to check the various extrapolations of this formula. These data points are selected by requiring that the predictions of eqn.IV.C.3 be at least twice as large as the predictions of eqn.IV.C.2. We find that the momentum extrapolation, that is, substitution I.D.8.c, provides the best fit to our very limited data set. Thus $S = \frac{\beta\gamma}{\alpha}$ is used in place of $\frac{\beta}{\alpha}$. Equation I.D.7 is multiplied by γ^2 to correct for the relativistic density of states. An effective target atomic number of $Z_T=0.3$ is used [ref.14], incorporating the Slater constant to correct for the fact that the two K-shell electrons tend to screen the nuclear potential and thus alter the K-shell wave functions. We again use Oppenheimer's multiplicative factor of 1.202 to account for attachment into excited states of the projectile. We thus use the following equation to predict non-radiative attachment cross sections.

$$\sigma_{nro} = 1.202 \gamma^2 \frac{\pi a_0^2}{5} 2^{18} Z_p^5 Z_T^5 S^8 \quad \text{IV.C.3}$$

$$\times [S^2 + (Z_p + Z_T)^2]^{-5} [S^2 + (Z_p - Z_T)^2]^{-5}$$

where $a_0 = 0.529 \times 10^{-8} \text{ cm}$, the Bohr radius,

$Z_P =$ *projectile atomic number,*

$Z_T = Z_T - 0.3$, *the effective charge of target, and*

$$S = \frac{\beta\gamma}{\alpha}.$$

The data set in which non-radiative processes dominate is compared to eqn.IV.C.3 in Fig.12. We note that the χ^2 for this calculation is ≈ 10 per degree of freedom and that substitution I.C.8.b (the kinetic energy substitution) gives a χ^2 value of more than 20/DOF. In the velocity regime for this data we see that there is little difference in the predictions of these two substitutions. Raisbeck et al. originally used the kinetic energy substitution to extrapolate the OBK formulation to relativistic energies [ref.33]. The substitution I.D.8.a for velocity becomes unphysical in the velocity regime of this data.

For some of our data neither attachment process is clearly dominant. We calculate the attachment cross section as

$$\sigma_a = \sigma_{ra} + \sigma_{rad} \quad \text{IV.C.4}$$

The χ^2 for the fit to all of our data is ≈ 1.6 . Predictions of eqn.IV.C.4 agree with measurements for low Z_T targets to within $\approx 20\%$. Discrepancies for the heavier targets are larger and may reflect contributions of capture from higher (e.g.L,M etc) shells of the target in the non-radiative case or the breakdown of the free electron assumption in the radiative case.

IV.D.Stripping cross sections

Values of the effective stripping cross sections obtained from our data are listed in Table 5. We also show the predictions of eqn.I.D.9 (BOHR 1), I.D.11 (IND SCAT) and I.D.12 (BOHR 2) as well as the value of $\alpha Z_T^2/\beta Z_P$, the semi-classical parameter which indicates whether the independent scatterer or screened potential approximation is applicable.

Formulations of the single electron stripping cross sections are discussed in Sec.I.D.2. We presented two separate equations for computing this cross section in the region of the independent scatterer approximation, generally valid for low Z_T targets. For high Z targets we have only the approximate formula from Bohr which is based on an exponential screening potential. Figure 11 shows the relative size of the cross section predicted by each of these equations for 400 MeV/nucleon Ne ions as a function of target charge.

For comparison with theory we make the division between low and high Z targets based on the predictions of eqn.I.D.11 and I.D.12 (which are reproduced below). We note that this division agrees with the division suggested by the value of $\alpha Z_T^2/\beta Z_p$. When screening is important, the predictions based on the independent scatterer approximation, eqn.I.D.11, will be too large. Thus we use the equation which gives the smallest value for the stripping cross section to determine the appropriate regime. Our so-called low Z data are the set of data for which predictions of eqn.I.D.11 are at least a factor of two smaller than the predictions of eqn.I.D.12. Our high Z data set requires predictions of eqn.I.D.12 to be at least a factor of two smaller than predictions of eqn.I.D.11. We first treat the case of low Z targets.

The Bohr formula for the independent scatterer approximation as given in Sec.I.D. is:

$$\sigma_s = 4\pi a_0^2 \left(\frac{\alpha}{Z_p\beta}\right)^2 (Z_T + Z_p) \quad \text{I.D.9}$$

The equation based on Mott and Massey's ionization cross sections for this case is

$$\sigma_s = \frac{4\pi a_0^2 \alpha^2}{Z^2 \beta^2} (Z_T^2 + Z_T) C_1 \left[\ln \frac{(4\beta^2 \gamma^2)}{(C_2 \alpha^2 Z_p^2)} - \beta^2 \right] \quad \text{I.D.11}$$

where $C_1 = 0.285$ and $C_2 = 0.048$. A comparison between these two equations and our low Z data is given in Fig.14 a and b where we plot the ratio of measured to calculated values for the cross section. We conclude from figure 14.a that the Bohr formula consistently underestimates the stripping cross section. The Mott and Massey form fits our data well, however, giving a χ^2 of ≈ 1 per degree of freedom and predicting the mean values to within 5% on the average. The

predictions of this equation are best in the region where $\alpha Z_T^2/\beta Z_p$ are much smaller than 1, suggesting that for values between 0.1 and 1 there may still be significant screening effects in the effective potential.

The only predictor we have for high Z targets is based on the approximate formula presented by Bohr. This is discussed in I.D.2 and given as

$$\sigma_s = \pi a_0^2 \frac{Z_T^3}{Z_p} \left(\frac{\alpha}{\beta} \right) \quad \text{I.D.12}$$

We have measured three stripping cross sections in the region where eqn.I.D.12 predicts values significantly (x2) smaller than I.D.11. The ratio of our measured values to the predictions of eqn.I.D.12 are shown in Fig.15. These data are all for Au targets. We note that the measurement for 140 Mev/nucleon C is low but that the predictions for the higher velocity (1050 and 2100 Mev/nucleon) Ne are close to perfect. The discrepancy for the C point may reflect a breakdown in the Born approximation since $\alpha Z_T/\beta > 1$ for that point.

We have not discussed a predictor for stripping cross sections in the region intermediate between the independent scatterer and screened potential limits. In this region we would expect our recipe for taking the smaller of the two predictions to break down. The real value will probably contain contributions from both extremes. Thus using the smaller value to calculate R_{eq} for the intermediate Z targets (as listed in Table 3) will underestimate the predicted ratio. This effect is seen in Fig.9 for the Ni,Cu,Ag and Ta targets.

V.Conclusions

We have presented the first measurements of single electron attachment and stripping cross sections for heavy ions at relativistic velocities. We have shown that the process of radiative electron attachment is clearly important at energies greater than 100 MeV/nucleon. Employing equations similar to those used by Raisbeck and Yiou [ref.4] and Wilson [ref.14], we can calculate these cross sections as the inverse of the photoionization process to within the

errors associated with our measurements, typically $\pm 20\%$. Measurements of the single electron attachment cross section for relativistic nuclei could thus provide a method of obtaining high energy photoionization cross sections.

We have also shown that the momentum extrapolation of the non-radiative Brinkman-Kramers formulation provides a reasonable predictor for the attachment cross sections in the region where the non-radiative process is dominant. Attachment cross sections predicted by the OBK formulation typically agree with the measured values to within a factor of two.

In addition, we have seen that the semi-classical formulation by Bohr for the stripping cross section in the regime of the independent scatterer approximation yields predictions which are low by a factor of two. The formulation of this cross section by Fowler et al. [ref.23] and by Wilson [ref.7] based on the ionization cross sections of Mott and Massey is able to predict values to within the experimental uncertainties, although it tends to overestimate values in the region where the screening parameter ($\alpha Z \hbar^2 / \beta Z_p$) is still smaller than 1. A measurement of stripping cross sections for gas targets would provide a better test of these ionization formulae since they would isolate stripping from the 1s state on which the calculations are based.

Finally, the predictions of Bohr's formula for the case where screening effects are important agree with our measured cross sections in that regime. We note that in the regime between the independent scatterer approximation and the fully screened potential approximation we have no sufficiently reliable predictor for the stripping cross section.

REFERENCES

1. V. S. Nikolaev, Sov. Phys. Usp. 8, 269 (1965).
2. N. Bohr and J. Linhard, Kgl. Danske Videnskab. Selskab, Mat.-Fys. Medd. 28, No. 7 (1954).
3. H. H. Heckman, Edward L. Hubbard, and William G. Simon, Phys. Rev. 129, 1240 (1963).
4. G. Raisbeck and F. Yiou, Phys. Rev. A 4, 1858 (1971).
5. R. H. Pratt, Akiva Ron, and H. K. Tseng, Rev. Mod. Phys. 45, 273 (1973).
6. F. Sauter, Ann. Phys. 9, 217 (1931).
7. Lance W. Wilson, Ph.D. thesis, University of California at Berkeley, Lawrence Berkeley Laboratory report LBL-7723.
8. M. Garrilla, Phys. Rev. 113, 514 (1959).
9. R. H. Pratt, Phys. Rev. 117, 1017 (1960).
10. Leonard I. Schiff, Quantum Mechanics, McGraw-Hill, Inc., 1968.
11. Hans-Dieter Betz, Rev. Mod. Phys. 44, 465 (1972).
12. J. R. Oppenheimer, Phys. Rev. 31, 349 (1928).
13. H. C. Brinkman and H. A. Kramers, Proc. Acad. Sci. Amsterdam 33, 973 (1930).
14. Lance W. Wilson, Proc. 15th Int. Cosmic Ray Conference, Plovdiv 2, 274 (1977).
15. J. C. Slater, Phys. Rev. 36, 51 (1930).
16. J. D. Jackson and Harry Schiff, Phys. Rev. 89, 359 (1953).
17. M. H. Mittleman, Proc. Phys. Soc. London 84, 453 (1964).
18. M. R. C. McDevell and J. P. Coleman, Introduction to the Theory of Atomic Ion Collisions, North Holland, Amsterdam, 1970.
19. N. Bohr, Kgl. Danske Videnskab. Selskab., Mat.-Fys. Medd. 18, No. 18 (1948).

20. I. S. Dmitriev, Ya. M. Zhileikin, and V. S. Nikolaev, *Sov. Phys. JETP* 22, 352 (1966).
21. N. F. Mott and H. S. W. Massey, The Theory of Atomic Collisions, Oxford University Press, London, 1965.
22. H. Bethe, *Ann. der Phys.* 5, 325 (1930).
23. P. H. Fowler, V. M. Clapham, V. G. Cohen, J. M. Kidd, and R. T. Moses, *Proc. Roy. Soc. London, Ser. A*: 318, 1 (1970).
24. Bevatron/Bevalac Users' Handbook, Lawrence Berkeley Laboratory report PUB-100 (1977).
25. D. E. Greiner, P. J. Lindstrom, F. S. Bieser, and H. H. Heckman, Lawrence Berkeley Laboratory report LBL-2107 (1972).
26. R. Harrower, Nuclear Science Division Annual Report, Lawrence Berkeley Laboratory report LBL-5075, p. 372 (1975).
27. J. T. Walton, H. A. Sommer, D. E. Greiner, and F. S. Bieser, *Proc. IEEE Trans. on Nuc. Sci.* 25, 391 (1978).
28. Stuart L. Meyer, Data Analysis for Scientists and Engineers, John Wiley and Sons, Inc., New York, 1975.
29. CAMAC, IEEE std. No. 583 (1975).
30. J. P. Chandler, computer code STEPIT (Dept. of Chemistry, Indiana University, Bloomington, IN, 1965).
31. J. K. Knipp and E. Teller, *Phys. Rev.* 59, 659 (1941).
32. Walter H. Barkas, Nuclear Research Emulsions, (Academic Press, New York, 1963), p. 371.
33. G. M. Raisbeck, H. J. Crawford, P. J. Lindstrom, D. E. Greiner, F. S. Bieser, and H. H. Heckman, *Proc. 15th Int. Cosmic Ray Conference, Plovdiv* 2, 67 (1977).

Table Captions

1. Table I indicates the scope of data available from this experiment. Symbols in each box indicate what quantities are available for that beam/energy/target combination. REQ indicates measurement of the equilibrium ratio, i.e. the limiting value for the ratio of single electron to fully stripped ions emerging from a thick target; σ_a and σ_s indicate measurements of the single electron attachment and stripping cross sections.
2. Listed are the $\alpha Z/\beta$ values for all elements and beam energies relevant to this experiment. This is the expansion parameter for the Born approximation encountered in most of the calculations discussed in the text. The quantity Z represents the K-shell electron velocity for a single electron ion of nuclear charge Ze .
3. Table 3 presents the equilibrium ratios, R_{eq} , measured in this experiment. We also list calculations of these ratios as $R_{eq} = \sigma_a/\sigma_s$ based on our best predictors for the attachment and stripping cross sections. The symbols RAD/IND indicate which theoretical formulation was used to calculate R_{eq} ; RAD indicates that the radiative process dominates the attachment cross section; NRA indicates dominance of the non-radiative attachment process; IND indicates that σ_s was calculated in the independent scatterer approximation (eqn. I.D.11); SCR indicates that σ_s was calculated using a screened potential approximation (eqn. I.D.12). Listed values of TEQ indicate the calculated thickness at which a measurement of R (the ratio of single electron ions to fully stripped ions) would yield a value of $0.9 R_{eq}$.

4. Values of the measured single electron attachment cross section per target atom, σ_a , are listed in Table 4. These values are grouped for each projectile (eg. ^{12}C) and incident energy (eg. 140 MeV/nucleon). Also listed are the calculated values for σ_a with a symbol to indicate which attachment process is dominant for that measurement: RAD (radiative) and NRA (non-radiative). Values calculated from eqn. IV.C.2 (radiative) and eqn. IV.C.3 (non-radiative) are included to provide a more complete comparison with theory.

5. Values of the measured single electron stripping cross section per target atom, σ_s , are given in Table 5. The values are grouped according to projectile and incident energy. We also list our calculated value for each cross section and indicate by symbol which assumption was used for the calculation: IND indicates the independent scatterer approximation was used (eqn. I.D.11); SCR indicates that the screened potential approximation was used (eqn. I.D.12). For comparison with theory we also list the predictions of each stripping cross section presented in the text: eqn. I.D.9 (BOHR1), eqn. I.D.11 (IND SCAT), and eqn. I.D.12 (BOHR2). We have listed values for $\alpha Z_T^2 / \beta Z_P$, the semi-classical parameter that indicates which potential approximation should be valid for calculating σ_s in each case.

DATA SUMMARY

PROJECTILE ${}^6\text{C}^{12}$				${}^{10}\text{Ne}^{20}$				${}^{18}\text{Ar}^{40}$	
MeV/nucleon	140	250	400	250	400	1050	2100	400	1050
TARGET									
1. ${}^4\text{Be}$	REQ	REQ	REQ	REQ	REQ	REQ	REQ	REQ σ_0, σ_s	REQ σ_0, σ_s
2. ${}^6\text{C}$		REQ σ_0, σ_s	REQ σ_0, σ_s			REQ σ_0, σ_s	REQ σ_0, σ_s	REQ σ_0, σ_s	REQ σ_0, σ_s
3. Mylar		REQ	REQ σ_0, σ_s	REQ σ_0, σ_s	REQ σ_0, σ_s	REQ σ_0, σ_s	REQ σ_0, σ_s	REQ σ_0, σ_s	REQ σ_0, σ_s
4. ${}^{13}\text{Al}$	REQ σ_0, σ_s	REQ σ_0, σ_s	REQ σ_0, σ_s	REQ σ_0, σ_s	REQ σ_0, σ_s	REQ σ_0, σ_s	REQ σ_0, σ_s	REQ σ_0, σ_s	REQ σ_0, σ_s
5. ${}^{28}\text{Ni}$		REQ		REQ	REQ	REQ		REQ	REQ
6. ${}^{29}\text{Cu}$	REQ	REQ	REQ σ_0, σ_s			REQ σ_0, σ_s	REQ σ_0, σ_s	REQ σ_0, σ_s	REQ σ_0, σ_s
7. ${}^{47}\text{Ag}$			REQ			REQ		REQ	REQ
8. ${}^{73}\text{To}$		REQ	REQ	REQ	REQ	REQ	REQ	REQ	
9. ${}^{79}\text{Au}$	REQ σ_0, σ_s	REQ	REQ			REQ σ_0, σ_s	REQ σ_0, σ_s	REQ σ_0, σ_s	REQ σ_0, σ_s

Table 1

$\alpha Z/\beta$ VALUES

ENERGY =		140	250	400	1050	2100 MeV/n
$\beta =$.494	.615	.715	.883	.952
${}_4\text{Be}$.059	.047	.041	.033	.031
${}_6\text{C}$.088	.071	.061	.049	.046
${}_{10}\text{Ne}$.148	.119	.102	.083	.077
${}_{13}\text{Al}$.192	.154	.133	.108	.100
${}_{18}\text{Ar}$.266	.214	.184	.149	.138
${}_{28}\text{Ni}$.413	.332	.286	.232	.215
${}_{29}\text{Cu}$.428	.344	.296	.240	.222
${}_{47}\text{Ag}$.694	.558	.480	.389	.361
${}_{73}\text{Ta}$		1.08	.866	.746	.604	.560
${}_{79}\text{Au}$		1.17	.937	.807	.653	.606

Table 2

EQUILIBRIUM RATIOS				
12C AT 140.MEV/NUC	R(MEASURED)	R(CALCULATED)	TEQ(MG/CM2)	
TARGET BE	2.99+/- .72X10 ⁻⁷	1.654E-07 RAD/IND	.3042	
TARGET AL	5.01+/- .94X10 ⁻⁷	5.898E-07 NRA/IND	.1001	
TARGET CU	1.73+/- .37X10 ⁻⁶	5.929E-06 NRA/SCR	.1187	
TARGET AU	5.51+/- .98X10 ⁻⁶	1.611E-06 NRA/SCR	.1886	
12C AT 250.MEV/NUC	R(MEASURED)	R(CALCULATED)	TEQ(MG/CM2)	
TARGET BE	5.64+/- .73X10 ⁻⁸	5.615E-08 RAD/IND	.4473	
TARGET C	4.35+/- .31X10 ⁻⁸	4.191E-08 RAD/IND	.2937	
TARGET MY	4.60+/- .60X10 ⁻⁸	4.205E-08 RAD/IND	.2644	
TARGET AL	4.28+/- .78X10 ⁻⁸	4.467E-08 NRA/IND	.1472	
TARGET CU	1.41+/- .18X10 ⁻⁷	3.780E-07 NRA/SCR	.1477	
TARGET NI	1.41+/- .18X10 ⁻⁷	3.409E-07 NRA/SCR	.1397	
TARGET TA	4.48+/- .58X10 ⁻⁷	9.482E-07 NRA/SCR	.2274	
TARGET AU	4.85+/- .63X10 ⁻⁷	7.942E-07 NRA/SCR	.2348	
12C AT 400.MEV/NUC	R(MEASURED)	R(CALCULATED)	TEQ(MG/CM2)	
TARGET BE	4.21+/- .62X10 ⁻⁸	2.251E-08 RAD/IND	.5795	
TARGET C	2.55+/- .34X10 ⁻⁸	1.691E-08 RAD/IND	.3675	
TARGET MY	3.19+/- .43X10 ⁻⁸	1.650E-08 RAD/IND	.3426	
TARGET AL	2.23+/- .41X10 ⁻⁸	1.011E-08 RAD/IND	.1907	
TARGET CU	4.26+/- .57X10 ⁻⁸	3.520E-08 NRA/SCR	.1716	
TARGET AG	7.49+/- 1.02X10 ⁻⁹	1.306E-07 NRA/SCR	.2112	
TARGET TA	1.39+/- .20X10 ⁻⁷	2.303E-07 NRA/SCR	.2641	
TARGET AU	1.60+/- .22X10 ⁻⁷	2.275E-07 NRA/SCR	.2727	
ZONE AT 250.MEV/NUC	R(MEASURED)	R(CALCULATED)	TEQ(MG/CM2)	
TARGET BE	1.91+/- .33X10 ⁻⁶	1.984E-06 RAD/IND	1.3871	
TARGET MY	1.49+/- .27X10 ⁻⁶	1.493E-06 RAD/IND	.8200	
TARGET AL	1.35+/- .18X10 ⁻⁶	1.639E-06 NRA/IND	.4564	
TARGET NI	4.26+/- .73X10 ⁻⁶	6.953E-06 NRA/SCR	.2329	
TARGET TA	1.27+/- .22X10 ⁻⁵	1.998E-05 NRA/SCR	.3789	
ZONE AT 400.MEV/NUC	R(MEASURED)	R(CALCULATED)	TEQ(MG/CM2)	
TARGET BE	7.87+/- .20X10 ⁻⁷	8.440E-07 RAD/IND	1.7887	
TARGET MY	6.85+/- 3.21X10 ⁻⁷	5.930E-07 RAD/IND	1.0575	
TARGET AL	4.14+/- 1.06X10 ⁻⁷	3.674E-07 RAD/IND	.5986	
TARGET NI	6.39+/- 1.62X10 ⁻⁷	6.915E-07 NRA/IND	.2871	
TARGET TA	2.40+/- .61X10 ⁻⁶	4.846E-06 NRA/SCR	.4402	

Table 3

EQUILIBRIUM RATIOS

ZONE AT 1050.MEV/NUC	R(MEASURED)	R(CALCULATED)	TEQ(MG/CM2)
TARGET BE	1.65+/- .23X10 -7	1.454E-07 RAD/IND	2.4736
TARGET C	1.19+/- .15X10 -7	1.039E-07 RAD/IND	1.5688
TARGET MY	1.21+/- .12X10 -7	1.308E-07 RAD/IND	1.4624
TARGET AL	5.01+/-2.41X10 -8	5.209E-08 RAD/IND	.8140
TARGET CJ	5.67+/- .76X10 -8	2.591E-08 RAD/IND	.4010
TARGET NI	5.91+/- .74X10 -8	2.559E-08 RAD/IND	.3970
TARGET AG	6.76+/- .95X10 -8	3.508E-08 RAD/SCR	.4347
TARGET TA	1.08+/- .13X10 -7	7.284E-08 NRA/SCR	.5437
TARGET AU	1.18+/- .15X10 -7	8.428E-08 NRA/SCR	.5615
ZONE AT 2100.MEV/NUC	R(MEASURED)	R(CALCULATED)	TEQ(MG/CM2)
TARGET BE	6.73+/- .88X10 -8	4.905E-08 RAD/IND	2.6472
TARGET C	4.92+/- .59X10 -8	3.504E-08 RAD/IND	1.6789
TARGET MY	5.31+/- .68X10 -8	3.399E-08 RAD/IND	1.5650
TARGET AL	3.24+/- .98X10 -8	1.752E-08 RAD/IND	.8711
TARGET CJ	1.75+/- .22X10 -8	8.186E-09 RAD/IND	.4292
TARGET TA	1.84+/- .17X10 -8	1.031E-08 RAD/SCR	.5862
TARGET AU	1.94+/- .23X10 -8	1.073E-08 RAD/SCR	.6054
40AR AT 400.MEV/NUC	R(MEASURED)	R(CALCULATED)	TEQ(MG/CM2)
TARGET BE	3.23+/- .39X10 -5	4.942E-05 RAD/IND	6.6455
TARGET C	2.30+/- .28X10 -5	3.559E-05 RAD/IND	4.2147
TARGET MY	2.26+/- .31X10 -5	3.476E-05 RAD/IND	3.6289
TARGET AL	1.45+/- .24X10 -5	2.180E-05 RAD/IND	2.1868
TARGET CJ	2.32+/- .47X10 -5	4.584E-05 NRA/IND	1.0774
TARGET NI	2.04+/- .26X10 -5	4.317E-05 NRA/IND	1.0666
TARGET AG	4.27+/- .52X10 -5	9.438E-05 NRA/IND	.7053
TARGET TA	6.92+/- .86X10 -5	1.557E-04 NRA/SCR	.7923
TARGET AU	8.08+/- .99X10 -5	1.551E-04 NRA/SCR	.8182
40AR AT 1050.MEV/NUC	R(MEASURED)	R(CALCULATED)	TEQ(MG/CM2)
TARGET BE	6.39+/- .83X10 -6	8.787E-06 RAD/IND	9.0656
TARGET C	4.75+/- .59X10 -6	6.277E-06 RAD/IND	5.7496
TARGET MY	5.00+/- .77X10 -6	6.091E-06 RAD/IND	5.3596
TARGET AL	3.07+/- .44X10 -6	3.148E-06 RAD/IND	2.9831
TARGET CJ	1.92+/- .52X10 -6	1.577E-06 RAD/IND	1.4697
TARGET NI	1.76+/- .25X10 -6	1.617E-06 RAD/IND	1.4550
TARGET AG	1.98+/- .10X10 -6	1.321E-06 RAD/IND	.9622
TARGET AU	3.52+/- .43X10 -6	2.690E-06 NRA/SCR	1.0107

ATTACHMENT CROSS SECTIONS (CM ² /ATOM)						
12C AT 140.MEV/NUC	SIGMA(MEASURED)	(CALCULATED)		RADIATIVE	NON-RADIATIVE	
TARGET AL	1.79+/- .43X10-25	6.071E-25	NRA	5.605E-26	5.510E-25	
TARGET AU	7.41+/-3.7CX10-24	6.422E-24	NRA	3.406E-25	6.062E-24	
12C AT 250.MEV/NUC	SIGMA(MEASURED)	(CALCULATED)		RADIATIVE	NON-RADIATIVE	
TARGET C	5.15+/-1.95X10-27	6.769E-27	RAD	6.415E-27	3.593E-28	
TARGET AL	1.42+/- .35X10-26	3.126E-26	NRA	1.390E-26	1.736E-26	
12C AT 400.MEV/NUC	SIGMA(MEASURED)	(CALCULATED)		RADIATIVE	NON-RADIATIVE	
TARGET C	2.54+/- .82X10-27	2.108E-27	RAD	2.090E-27	1.916E-29	
TARGET MY	1.64+/- .52X10-26	1.767E-26	RAD	1.742E-26	2.520E-28	
TARGET AL	6.61+/-1.32X10-27	5.463E-27	RAD	4.529E-27	9.345E-28	
TARGET CU	2.71+/-1.48X10-26	4.977E-26	NRA	1.010E-26	3.966E-26	
20NE AT 250.MEV/NUC	SIGMA(MEASURED)	(CALCULATED)		RADIATIVE	NON-RADIATIVE	
TARGET MY	4.81+/-3.45X10-25	6.682E-25	RAD	6.089E-25	5.930E-26	
TARGET AL	2.60+/- .81X10-25	3.700E-25	NRA	1.583E-25	2.117E-25	
20NE AT 400.MEV/NUC	SIGMA(MEASURED)	(CALCULATED)		RADIATIVE	NON-RADIATIVE	
TARGET MY	1.34+/- .92X10-25	2.057E-25	RAD	2.026E-25	3.138E-27	
TARGET AL	5.16+/-2.65X10-26	6.432E-26	RAU	5.267E-26	1.164E-26	
20NE AT 1050.MEV/NUC	SIGMA(MEASURED)	(CALCULATED)		RADIATIVE	NON-RADIATIVE	
TARGET C	3.52+/-1.06X10-27	3.035E-27	RAD	3.034E-27	3.528E-31	
TARGET MY	3.14+/- .69X10-26	2.529E-26	RAD	2.528E-26	4.925E-30	
TARGET AL	7.89+/-1.30X10-27	6.593E-27	RAD	6.574E-27	1.900E-29	
TARGET CU	2.09+/- .53X10-26	1.568E-26	RAD	1.467E-26	1.014E-27	
TARGET AU	1.76+/- .79X10-25	1.129E-25	NRA	3.995E-26	7.296E-26	
20NE AT 2100.MEV/NUC	SIGMA(MEASURED)	(CALCULATED)		RADIATIVE	NON-RADIATIVE	
TARGET C	1.23+/- .58X10-27	9.563E-28	RAD	9.563E-28	2.061E-33	
TARGET MY	8.64+/-1.37X10-27	7.969E-27	RAO	7.969E-27	2.882E-32	
TARGET AL	2.15+/- .32X10-27	2.072E-27	RAD	2.072E-27	1.124E-31	
TARGET CU	6.37+/-1.62X10-27	4.628E-27	RAD	4.622E-27	6.384E-30	
TARGET AU	2.68+/-1.03X10-26	1.333E-26	RAD	1.259E-26	7.390E-28	
40AR AT 400.MEV/NUC	SIGMA(MEASURED)	(CALCULATED)		RADIATIVE	NON-RADIATIVE	
TARGET BE	2.07+/- .82X10-25	2.559E-25	RAO	2.554E-25	4.44CE-28	
TARGET C	3.74+/-1.12X10-25	3.869E-25	RAO	3.831E-25	3.818E-27	
TARGET MY	2.81+/- .91X10-24	3.246E-24	RAO	3.193E-24	5.300E-26	
TARGET AL	8.66+/-1.09X10-25	1.027E-24	RAO	8.301E-25	1.970E-25	
TARGET CU	4.35+/- .85X10-24	1.032E-23	NRA	1.852E-24	8.473E-24	
TARGET AU	7.56+/-1.96X10-23	1.426E-22	NRA	5.044E-24	1.375E-22	
40AR AT 1050.MEV/NUC	SIGMA(MEASURED)	(CALCULATED)		RADIATIVE	NON-RADIATIVE	
TARGET BE	3.69+/-1.22X10-26	3.335E-26	RAO	3.335E-26	7.449E-31	
TARGET C	4.55+/-1.39X10-26	5.003E-26	RAO	5.002E-26	6.445E-30	
TARGET MY	4.08+/- .59X10-25	4.169E-25	RAO	4.169E-25	8.959E-29	
TARGET AL	1.09+/- .17X10-25	1.097E-25	RAO	1.084E-25	3.472E-28	
TARGET CU	2.64+/- .46X10-25	2.603E-25	RAO	2.418E-25	1.855E-26	
TARGET AU	2.84+/- .71X10-24	2.002E-24	NRA	6.588E-25	1.344E-24	

Table 4

STRIPPING CROSS SECTIONS (ICP2/ATOM)

12C AT 140.MEV/NUC	SIGMA(MEASURED)	(CALCULATED)	BOHR1	IND SCAT	BOHR2	$\alpha Z_T^2/\beta Z_P$	
TARGET AL	3.37/-1.20X10-19	1.029E-18	IND	3.881E-19	1.029E-18	1.197E-18	.416
TARGET AU	1.34/-0.84X10-19	3.987E-18	SCR	1.348E-17	3.374E-17	3.987E-18	13.363
12C AT 250.MEV/NUC	SIGMA(MEASURED)	(CALCULATED)	BOHR1	IND SCAT	BOHR2		
TARGET C	1.18/-1.44X10-19	1.613E-19	IND	5.781E-20	1.613E-19	5.745E-19	.871
TARGET AL	3.31/-1.27X10-19	7.000E-19	IND	2.505E-19	7.000E-19	9.820E-19	.334
12C AT 400.MEV/NUC	SIGMA(MEASURED)	(CALCULATED)	BOHR1	IND SCAT	BOHR2		
TARGET C	1.02/-0.37X10-19	2.247E-19	IND	4.284E-20	1.247E-19	4.946E-19	.061
TARGET MY	5.14/-2.12X10-19	1.071E-18	IND	3.680E-19	1.071E-18	4.266E-18	.109
TARGET AL	2.47/-0.98X10-19	5.403E-19	IND	1.857E-19	5.403E-19	8.282E-19	.288
TARGET CU	8.26/-4.12X10-19	1.414E-18	SCR	8.075E-19	2.383E-18	1.414E-18	1.432
ZONE AT 250.MEV/NUC	SIGMA(MEASURED)	(CALCULATED)	BOHR1	IND SCAT	BOHR2		
TARGET MY	3.23/-2.75X10-19	4.474E-19	IND	1.787E-19	4.474E-19	2.975E-18	.076
TARGET AL	1.92/-0.73X10-19	2.257E-19	IND	9.018E-20	2.257E-19	5.772E-19	.201
ZONE AT 400.MEV/NUC	SIGMA(MEASURED)	(CALCULATED)	BOHR1	IND SCAT	BOHR2		
TARGET MY	1.96/-2.10X10-19	3.470E-19	IND	1.325E-19	3.470E-19	2.560E-18	.065
TARGET AL	1.25/-0.83X10-19	1.750E-19	IND	6.684E-20	1.750E-19	4.569E-19	.173
ZONE AT 1050.MEV/NUC	SIGMA(MEASURED)	(CALCULATED)	BOHR1	IND SCAT	BOHR2		
TARGET C	2.95/-0.97X10-20	2.921E-20	IND	1.011E-20	2.921E-20	2.402E-19	.030
TARGET MY	2.60/-0.71X10-19	2.509E-19	IND	6.683E-20	2.509E-19	2.072E-18	.053
TARGET AL	9.85/-4.06X10-20	1.266E-19	IND	4.381E-20	1.266E-19	4.023E-19	.140
TARGET CU	3.69/-1.30X10-19	6.051E-19	IND	2.094E-19	6.051E-19	6.868E-19	.696
TARGET AU	1.51/-0.80X10-18	1.340E-18	SCR	1.521E-18	4.395E-18	1.340E-18	5.161
ZONE AT 2100.MEV/NUC	SIGMA(MEASURED)	(CALCULATED)	BOHR1	IND SCAT	BOHR2		
TARGET C	2.50/-0.83X10-20	2.729E-20	IND	8.696E-21	2.729E-20	2.228E-19	.028
TARGET MY	1.63/-0.40X10-19	2.344E-19	IND	7.469E-20	2.344E-19	1.922E-18	.049
TARGET AL	6.75/-2.69X10-20	1.183E-19	IND	3.768E-20	1.183E-19	3.731E-19	.130
TARGET CU	3.63/-1.23X10-19	5.654E-19	IND	1.801E-19	5.654E-19	6.370E-19	.645
TARGET AU	1.58/-0.63X10-18	1.242E-18	SCR	1.309E-18	4.107E-18	1.242E-18	4.787
40AR AT 400.MEV/NUC	SIGMA(MEASURED)	(CALCULATED)	BOHR1	IND SCAT	BOHR2	$\alpha Z_T^2/\beta Z_P$	
TARGET SE	6.62/-3.25X10-21	5.177E-21	IND	2.267E-21	5.177E-21	1.258E-19	.009
TARGET C	1.52/-0.53X10-20	1.087E-20	IND	4.740E-21	1.087E-20	1.645E-19	.020
TARGET MY	1.24/-0.34X10-19	9.339E-20	IND	4.689E-20	9.339E-20	1.423E-18	.036
TARGET AL	5.99/-1.45X10-20	4.711E-20	IND	2.063E-20	4.711E-20	2.761E-19	.095
TARGET CU	1.87/-0.67X10-19	2.252E-19	IND	9.861E-20	2.252E-19	4.713E-19	.477
TARGET AU	9.10/-3.05X10-19	9.195E-19	SCR	7.183E-19	1.656E-18	9.193E-19	3.542
40AR AT 1050.MEV/NUC	SIGMA(MEASURED)	(CALCULATED)	BOHR1	IND SCAT	BOHR2		
TARGET SE	5.78/-2.48X10-21	3.795E-21	IND	1.486E-21	3.795E-21	1.019E-19	.007
TARGET C	9.58/-3.15X10-21	7.470E-21	IND	3.120E-21	7.470E-21	1.335E-19	.017
TARGET MY	3.16/-0.77X10-20	6.846E-20	IND	2.280E-20	6.846E-20	1.151E-18	.029
TARGET AL	3.55/-0.95X10-20	3.454E-20	IND	1.352E-20	3.454E-20	2.235E-19	.078
TARGET CU	1.38/-0.57X10-19	1.051E-19	IND	6.463E-20	1.051E-19	2.816E-19	.386
TARGET AU	8.06/-2.56X10-19	7.442E-19	SCR	4.695E-19	1.199E-18	7.442E-19	2.867

Table 5

Figure Captions

1. Experimental setup.
 - 1a. Spectrometer diagram showing target area (F3), two sets of quadrupole focusing systems, bending magnet, vacuum tank, and experimental cave.
 - 1b. Detail of experimental cave showing detector telescope, spectrometer rail, beam fluence monitor (SEM), beam steering monitor and single particle counter (RTOT).
 - 1c. Head-on view of detector telescope for counting single electron ions and of beam fluence monitor (SEM). Also shown are the focused beam spot size and the fully stripped ion beam spot size.
2. Electronics diagram for experiment.
3. Electronics diagram for scintillator backup experiment.
4. Pulse height distribution for a single detector (D1) from 400 MeV/nucleon Ne. This distribution is the basis of the maximum likelihood method used to identify individual ions.
5. Growth curve fit to six data points for 400 MeV/nucleon Ar passing through thin Mylar foils. The curve shown is $R = \sigma_a / \sigma_s (1 - e^{-\sigma_s x})$ where σ_a and σ_s are the most probable values for the attachment and stripping cross sections obtained by the method described in sec. III.H in the text. The target thickness, x , is converted from mg/cm² to atoms/cm² by multiplying 6.023 10²⁰/96. The χ^2 value for this fit (actually from eqn. III.H.2) is 0.6 per degrees of

freedom.

6. The distribution of the fitting statistic f (eqn. III.H.2) per degree of freedom (4) from 1000 simulated data sets based on our measurements for six targets for 400 MeV/nucleon Ar ions passing through Mylar foils. The Monte Carlo method used to generate this figure is described in sec. III.J of the text.
7. Distributions of σ_a' , σ_s' , and R_{eq}' obtained by fitting 1000 simulated data sets based on 400 MeV/nucleon Ar + Mylar measurements as described in sec. III.J of the text.
- 7a. Single electron attachment cross sections, σ_a' . Also shown is the best value, σ_a , obtained from the actual data set and its assigned error.
- 7b. Single electron stripping cross sections, σ_s' . Also shown is the best value obtained from the actual data and its assigned error.
- 7c. Equilibrium ratios, $R_{eq}' = \sigma_a'/\sigma_s'$. Also shown is the best value obtained from the actual data and its assigned uncertainty.
8. Comparison of measured equilibrium ratios with calculations based on equations presented in the text (see sec. IV.B). Plotted is the ratio $\frac{R_{eq}(\text{measured})}{R_{eq}(\text{calculated})}$ as a function of target. Each target may have up to nine values plotted, one for each beam/energy combination studied. The theoretical formulations used to compute each ratio are shown in Table 3.
9. Equilibrium ratios for Ne ions at four energies as a function of

target atomic number. The shape of the curve at each energy is due principally to the target dependence of the attachment cross section.

10. Energy dependence of the single electron attachment cross section for fully stripped Ne projectiles passing through Al foils. The curves are based on eqn. IV.C.2 (RAD), and eqn IV.C.3 (NON-RAD) showing the contribution to the predicted cross section (SUM) from radiative and non-radiative attachment processes. These parameter free theoretical formulations are discussed in sec. I.D and I.C in the text.
11. Comparison of measured and calculated attachment cross sections as a function of target for data in which the radiative attachment process is clearly dominant. Each target may have up to nine separate values, one for each beam/energy combination studied. No attachment cross sections were measured for the Ni, Ag, or Ta targets. See sec. IV.C for a description of the data selection procedure for this figure.
12. Comparison of measured and calculated attachment cross sections as a function of target for data in which the non-radiative attachment process dominates. Calculations are based on the momentum extrapolation of the Oppenheimer-Brinkman-Kramers formulation discussed in sec. I.D.
13. Energy dependence of the single electron stripping cross section for Ne⁺⁹ ions passing through thin Al foils. The curves are calculations based on eqn. I.D.9 (Bohr theory for independent

scattering), eq. I.D.11 (based on Mott and Masey ionization cross sections for independent scatterers) and eqn. I.D.12 (Bohr theory for screened potentials). The eqn. I.D.11 provides the best fit to our data but generally overestimates the cross sections, possibly because the independent scatterer approximation is not really valid unless $\sigma Z_T / \beta Z_p < 0.1$ (see discussion of sec. I.D).

14. Comparison of measurements with calculations for data in which the independent scatterer approximation provides the best description of the stripping process. Plotted is the ratio of measured single electron stripping cross section to the calculation based on eqn. I.D.11. Each target may have up to nine separate measured values, one for each beam/energy combination investigated.
- 14a. Comparison with Bohr theory in the independent scatterer approximation. This theory tends to underestimate cross sections by \sim a factor of 2.
- 14b. Comparison with stripping cross sections based on Mott and Massey ionization cross sections. This formulation tends to slightly overestimate cross sections as described in sec. IV.D. of text.
15. Comparison of measured and calculated single electron stripping cross sections in the region where the screened potential approximation provides the best description of the data. Calculations are based on eqn. I.D.12 from Bohr. We note that the 140 MeV/nucleon C point may be low because $\sigma Z_T / \beta > 1$ (see sec. IV.D in text). Data selection is discussed in sec. IV.D.

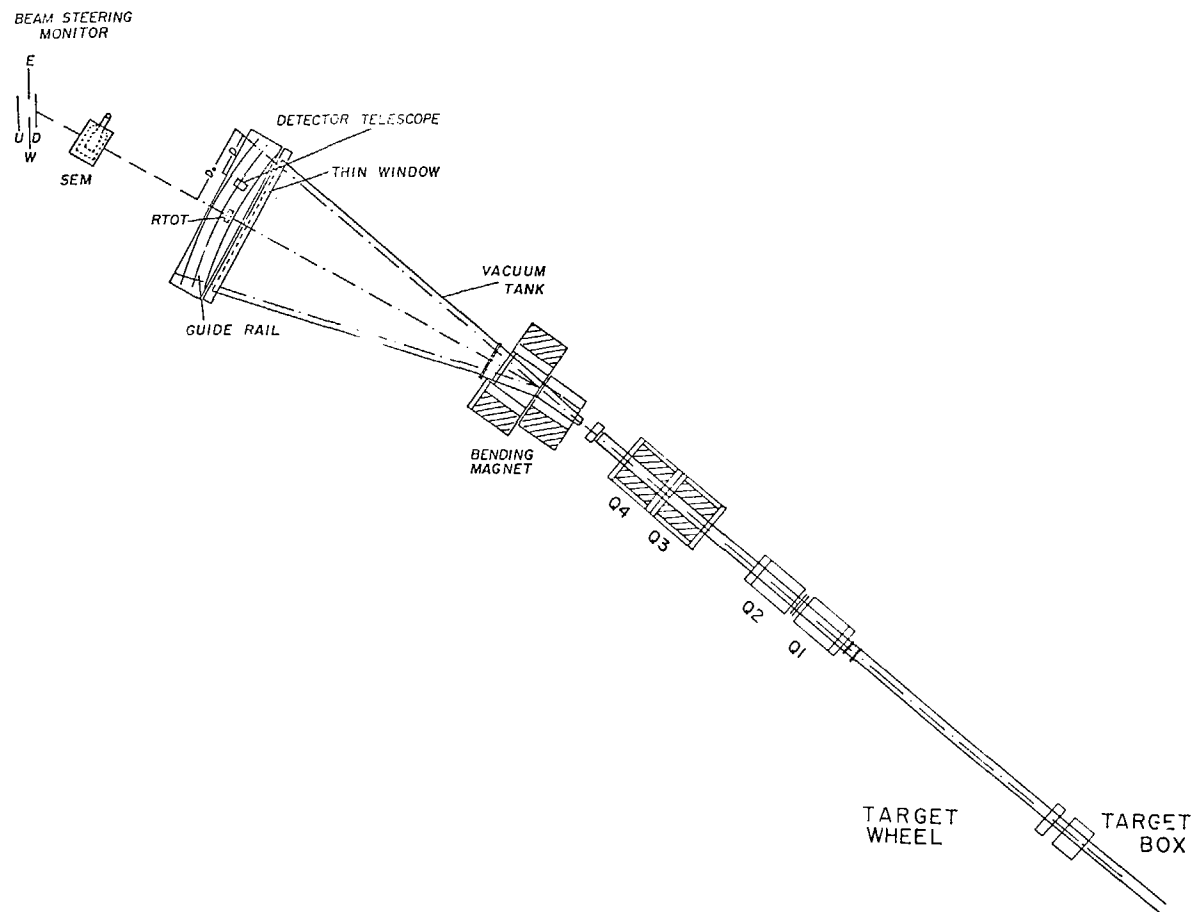
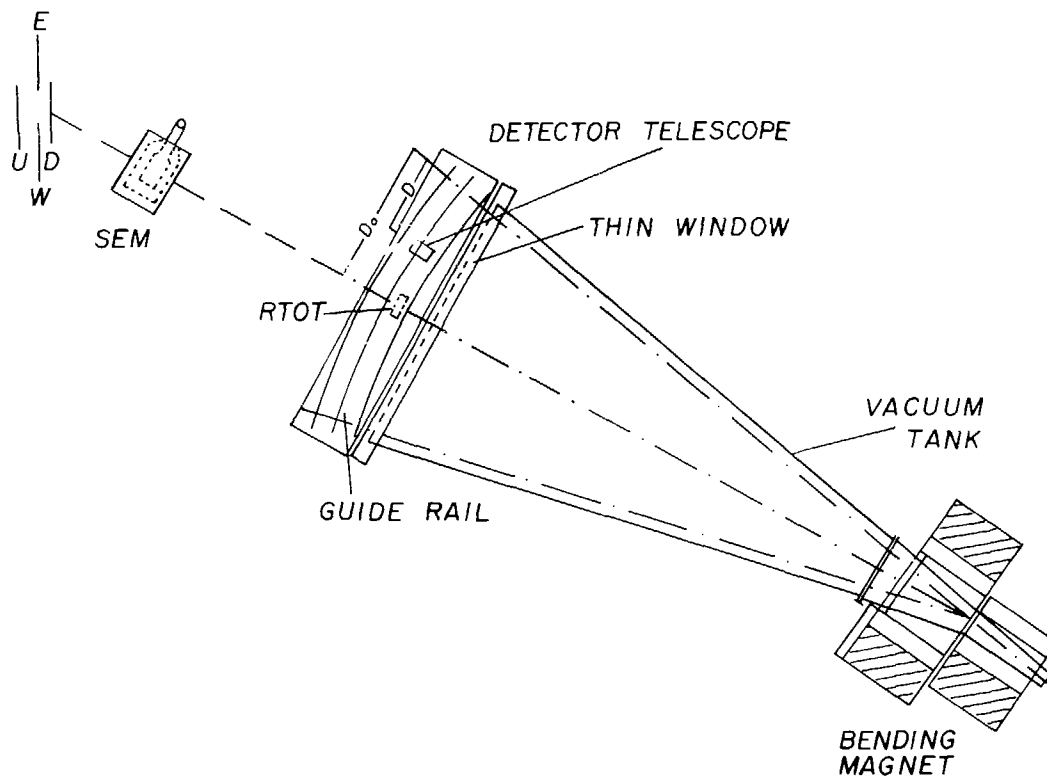


Fig 1a

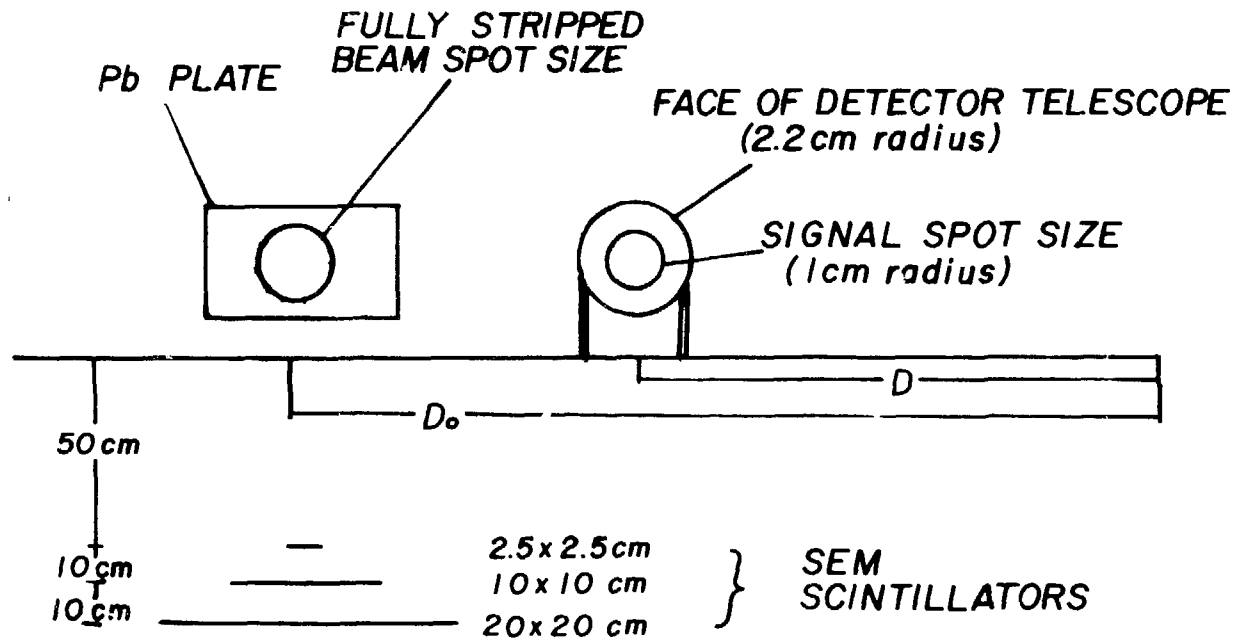
XBL 664-9263

BEAM STEERING MONITOR



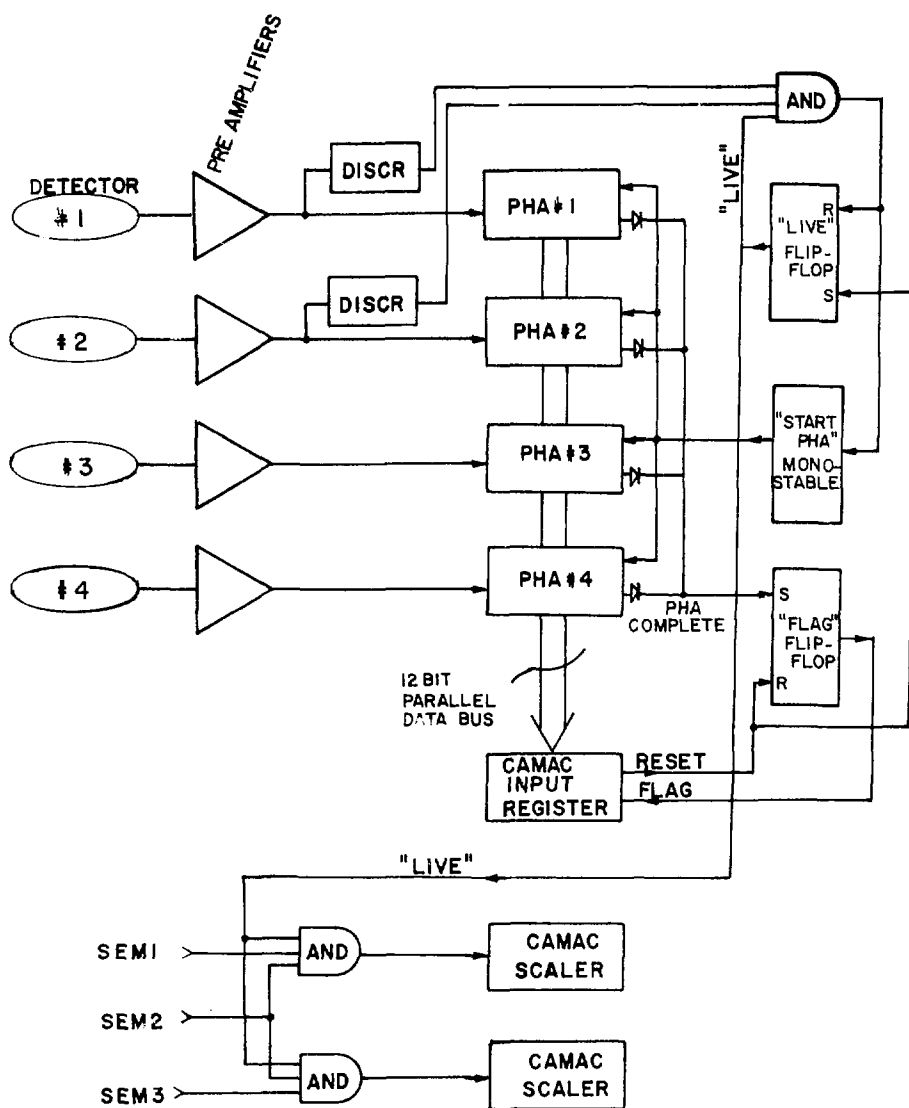
XBL 804-9264

Fig. 1b



XBL 804-9262

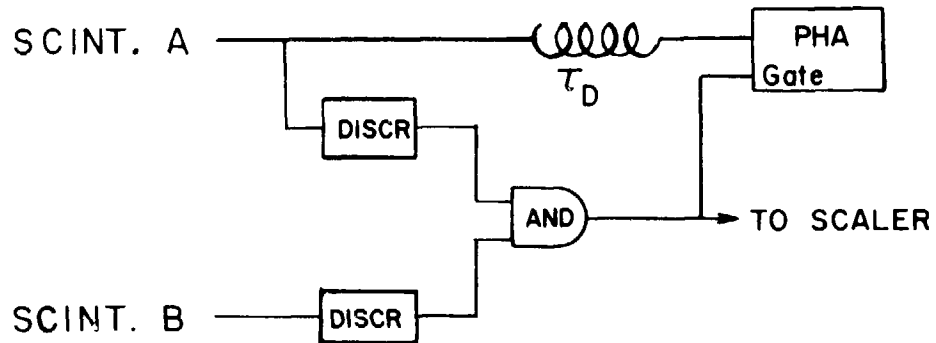
Fig. 1c



XBL 804-9266

Fig. 2

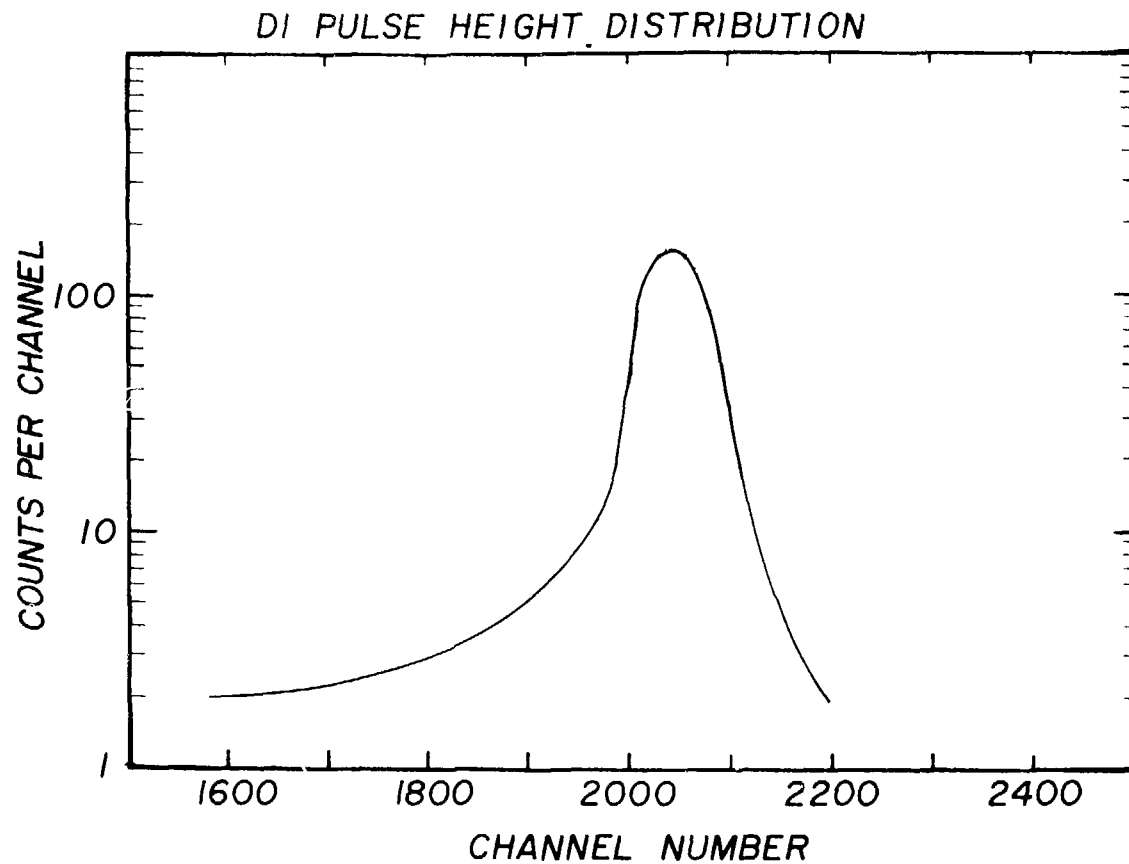
ELECTRONICS DIAGRAM



BACK UP EXPERIMENT

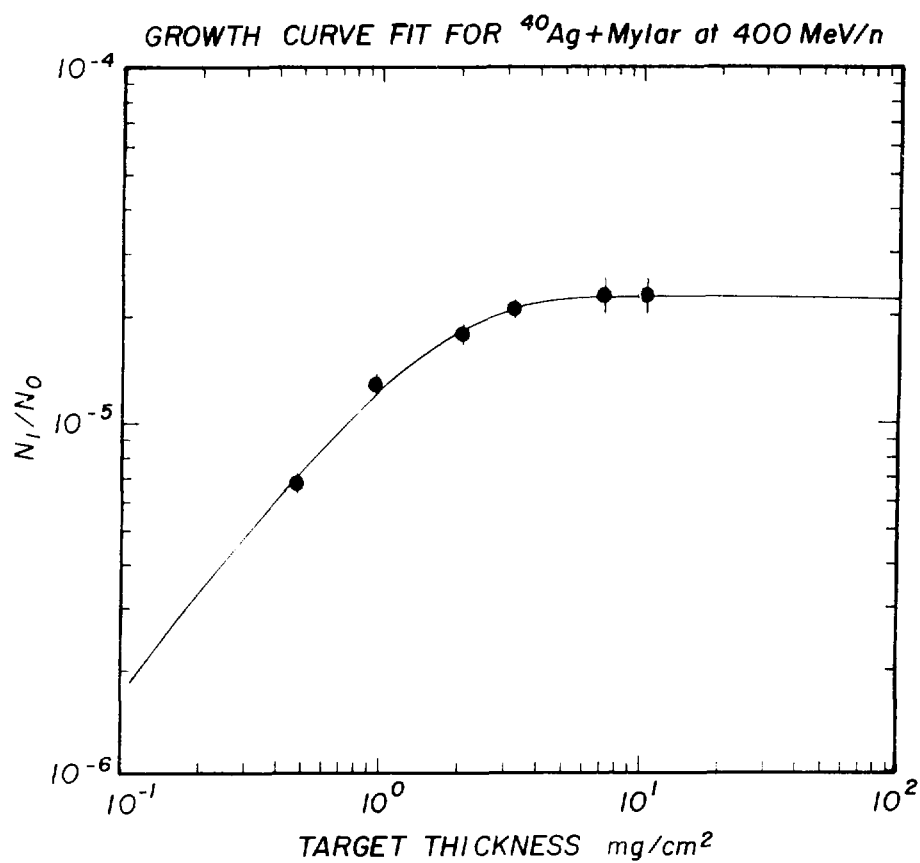
XBL 804-9261

Fig. 3



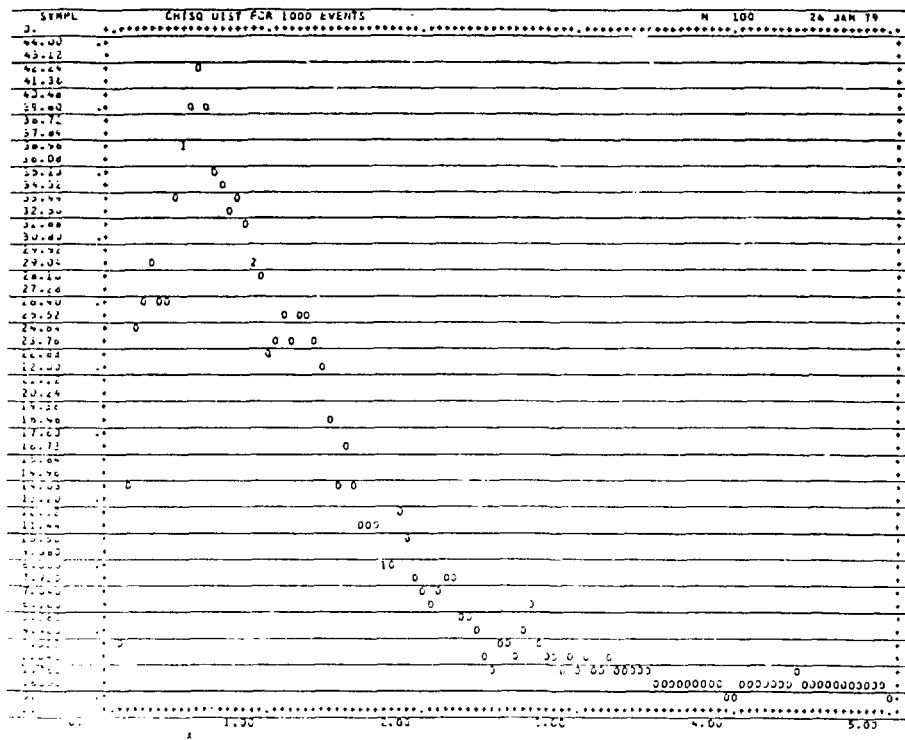
XBL 804-9260

Fig. 4



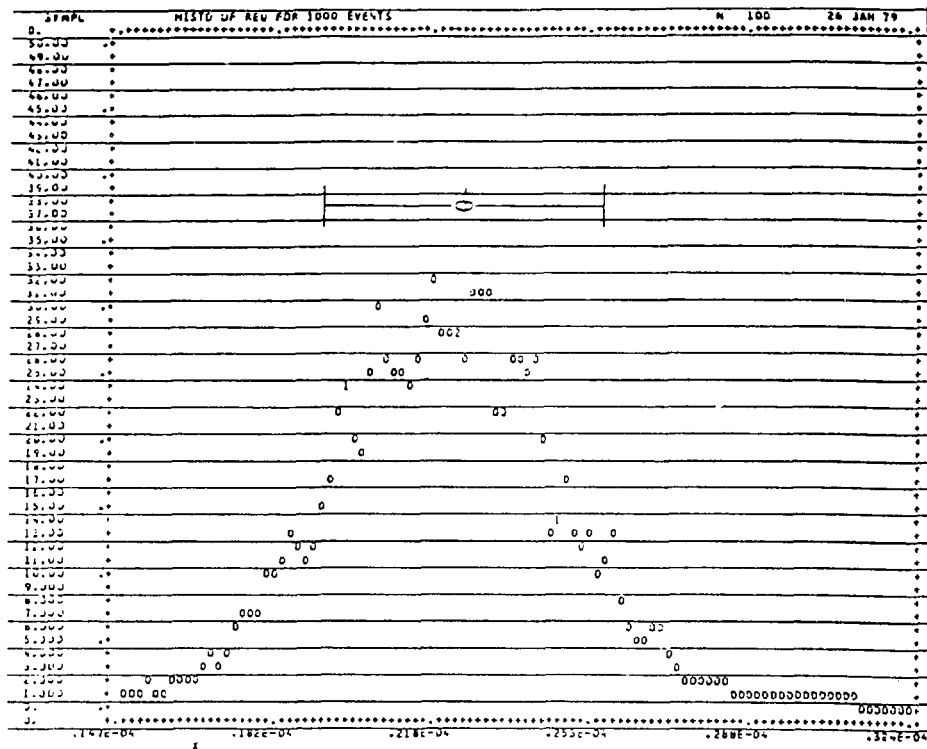
15L 404-9287

Fig. 5



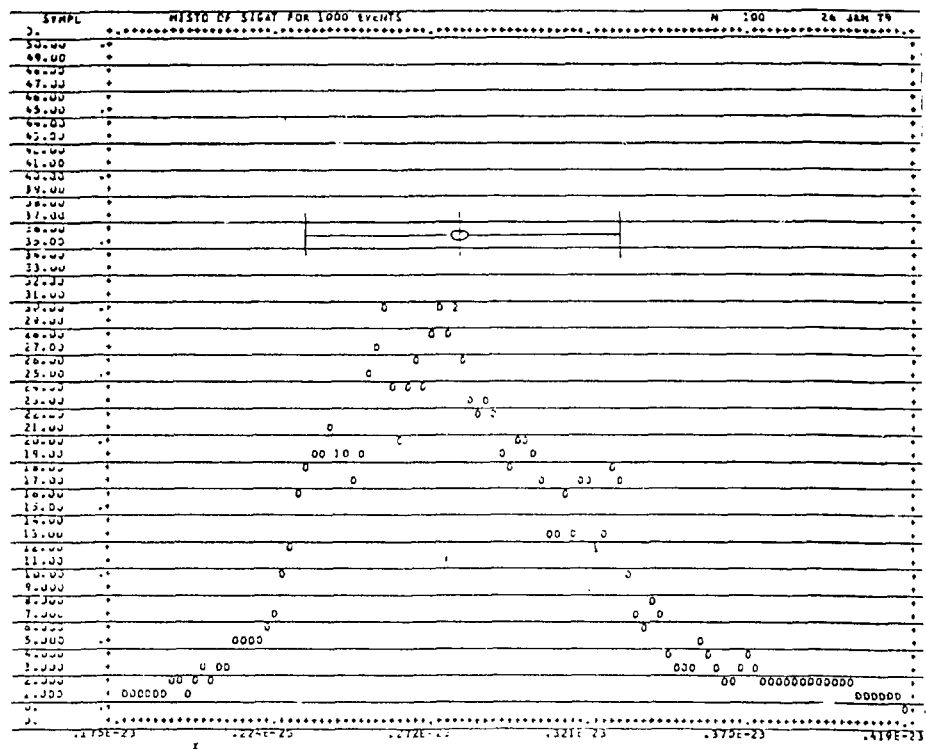
XBL 804-9242

Fig. 6



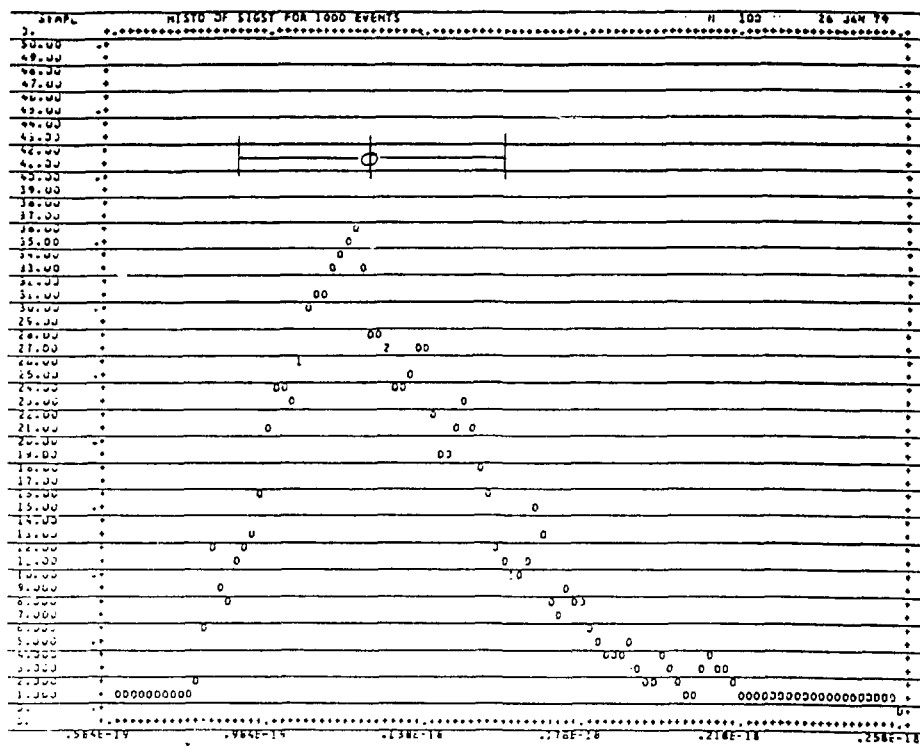
XBL 804-9243

Fig. 7a



XBL 804-9244

Fig. 7b



XBL 804-9245

Fig. 7c

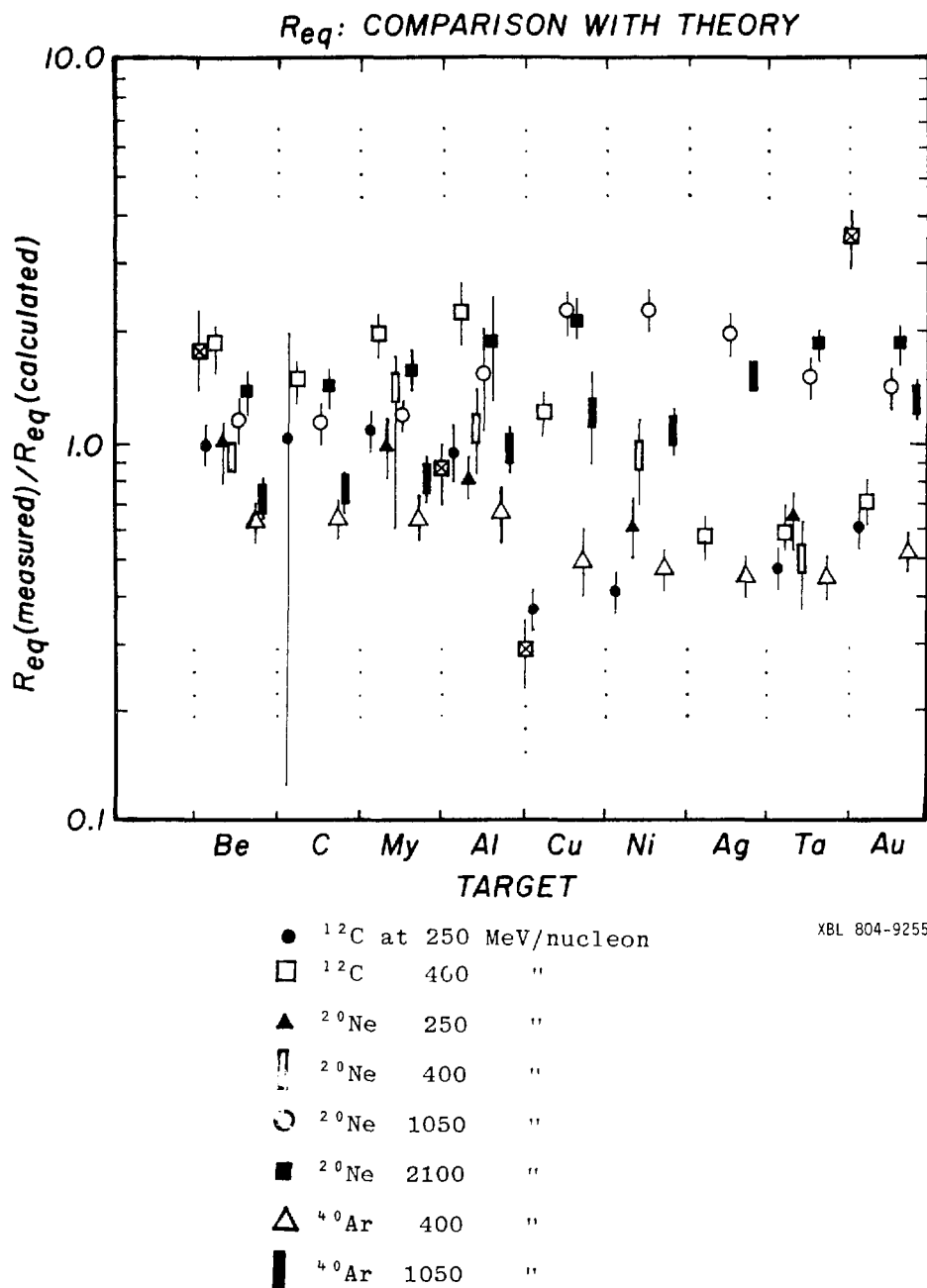
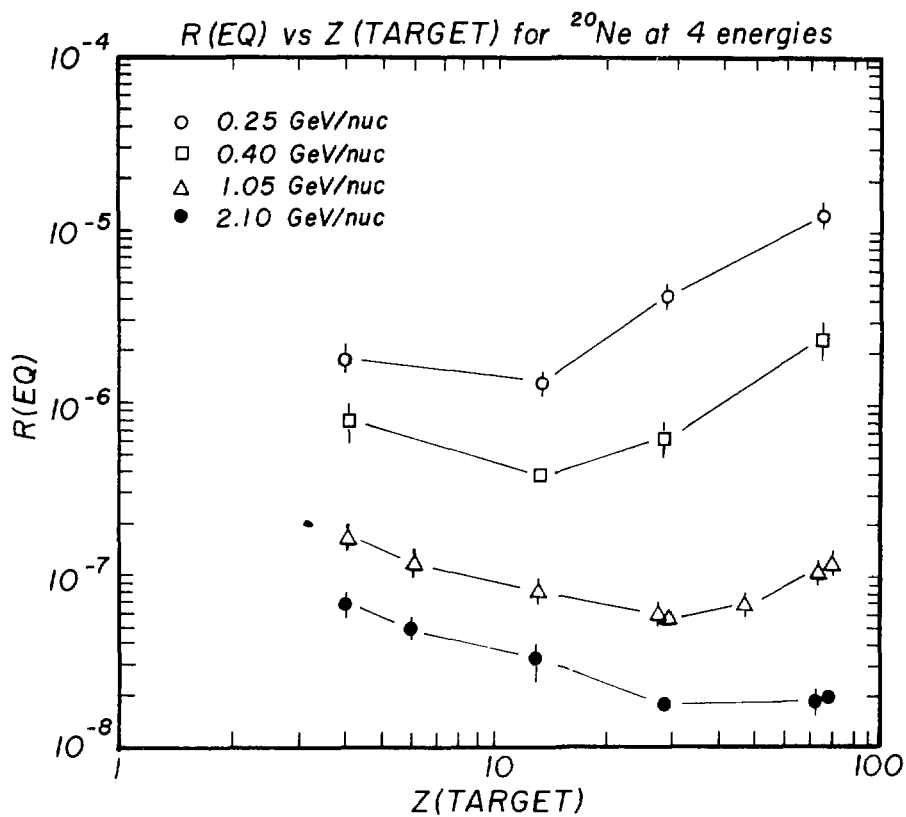
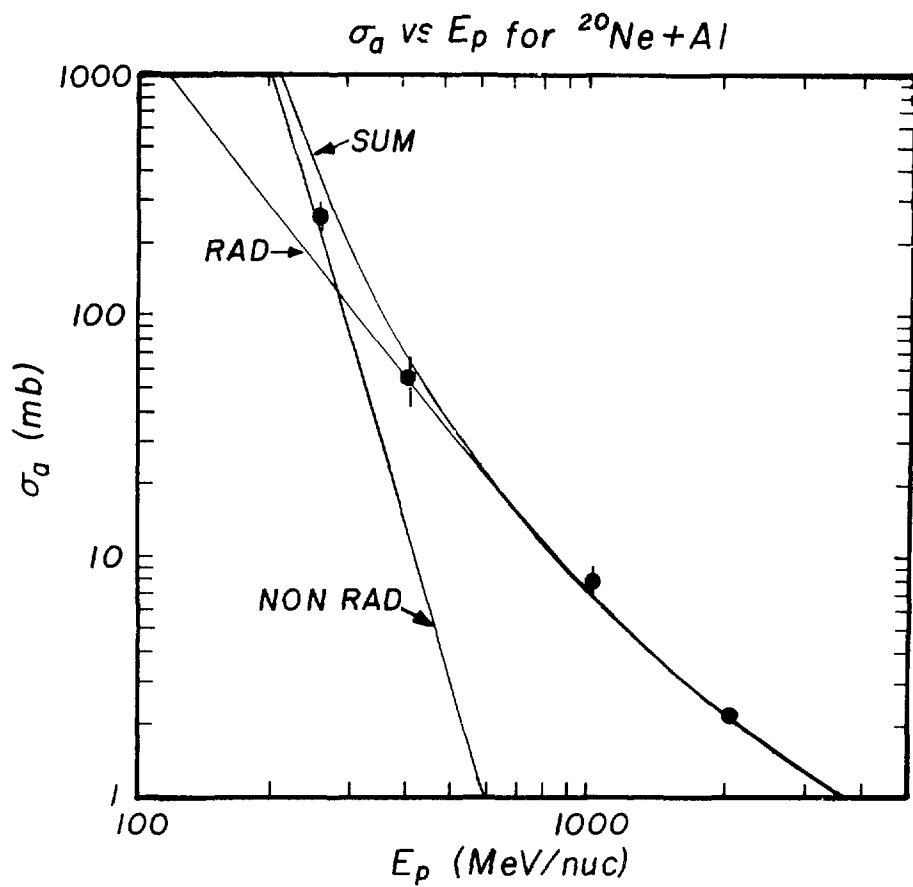


Fig. 8



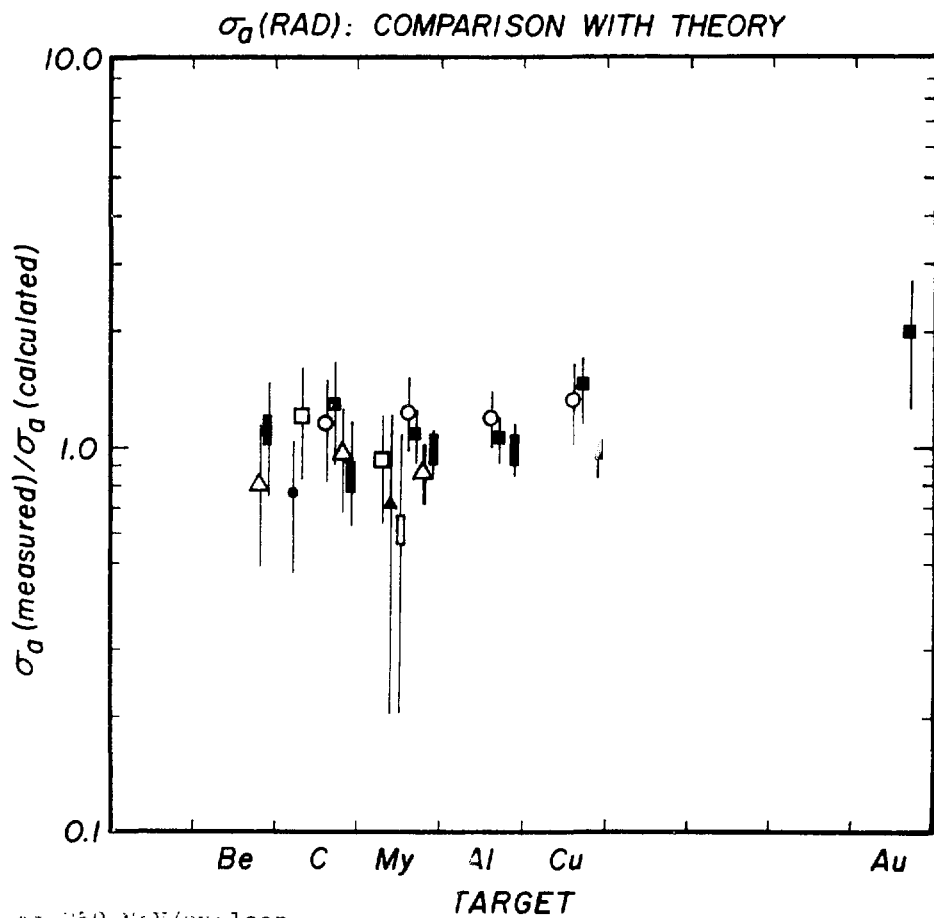
XBL 804-9265

Fig. 9



XBL 804-9256

Fig. 10



- ^2He at 250 MeV/nucleon
- ^{12}C 400 "
- ▲ ^{20}Ne 250 "
- ▤ ^{20}Ne 400 "
- ^{20}Ne 1050 "
- ^{20}Ne 2100 "
- △ ^{40}Ar 400 "
- ▥ ^{40}Ar 1050 "

XBL 804-9258

Fig. 11

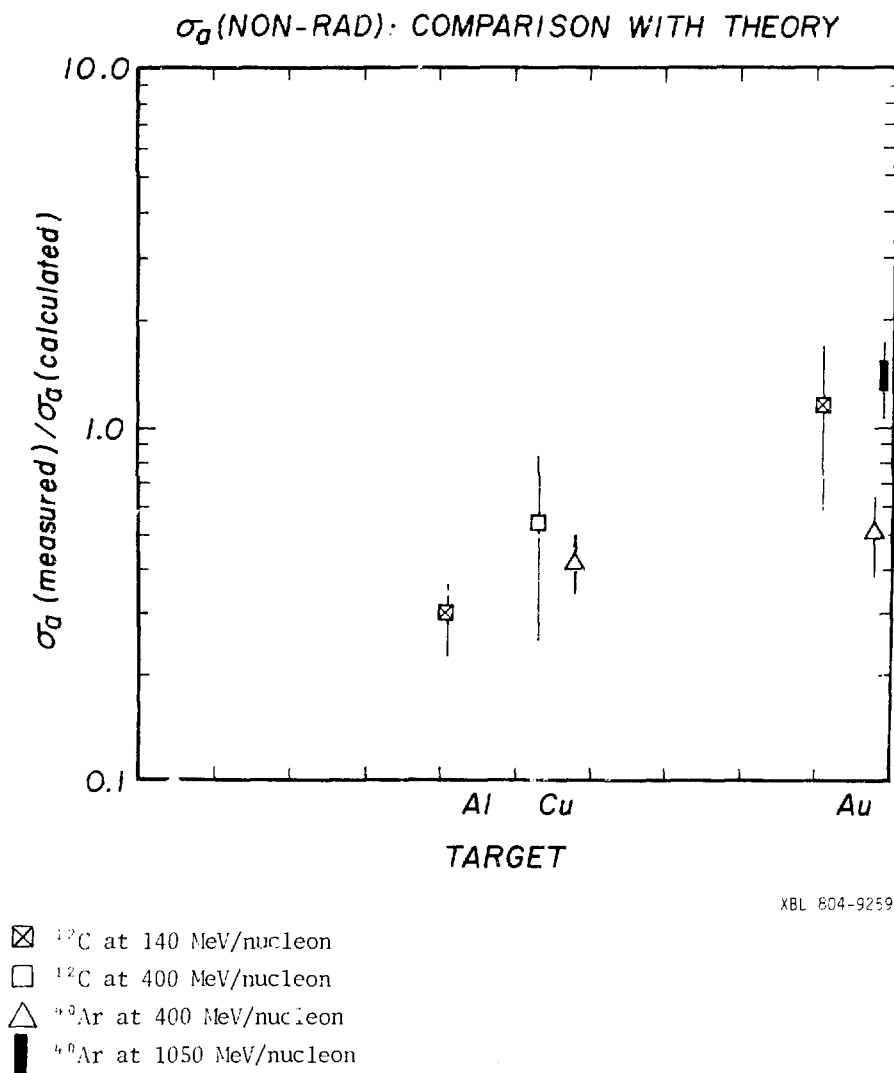
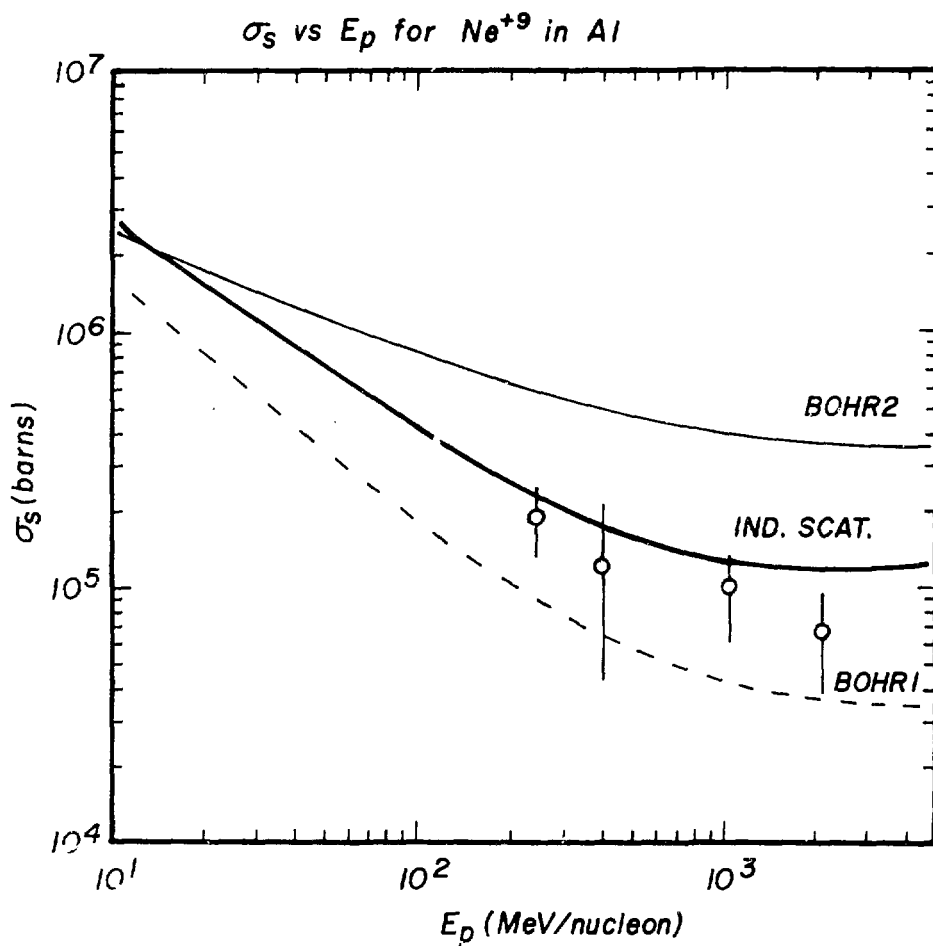
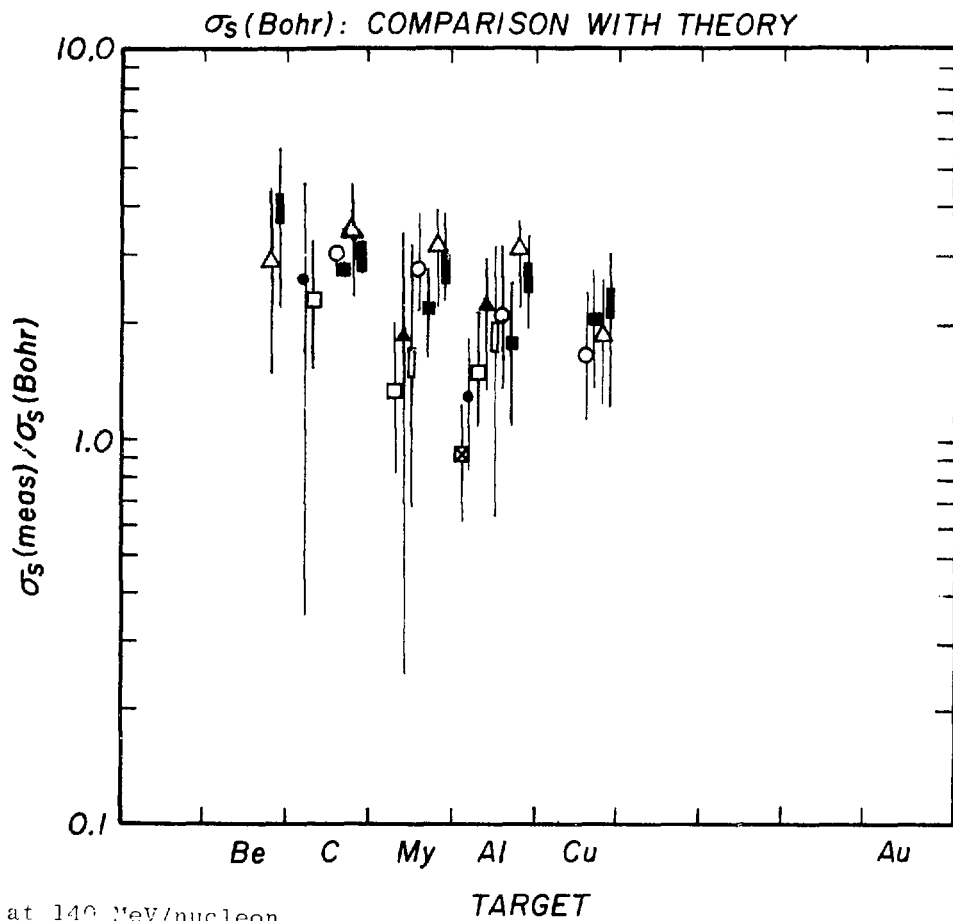


Fig. 12



XBL 804-9254

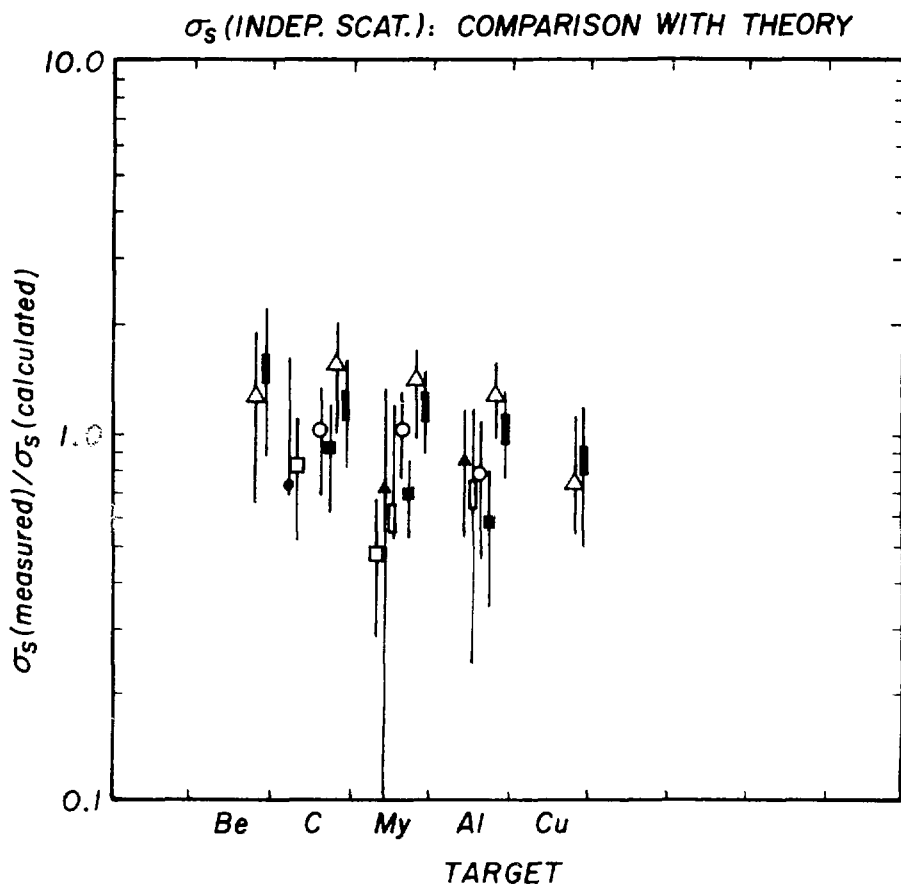
Fig. 13



- ⊠ ^{12}C at 140 MeV/nucleon
- ^{12}C at 250 MeV/nucleon
- ^{12}C 400 "
- ▲ ^{20}Ne 250 "
- ▤ ^{20}Ne 400 "
- ^{20}Ne 1050 "
- ^{20}Ne 2100 "
- △ ^{40}Ar 400 "
- ▥ ^{40}Ar 1050 "

XBL 804-9253

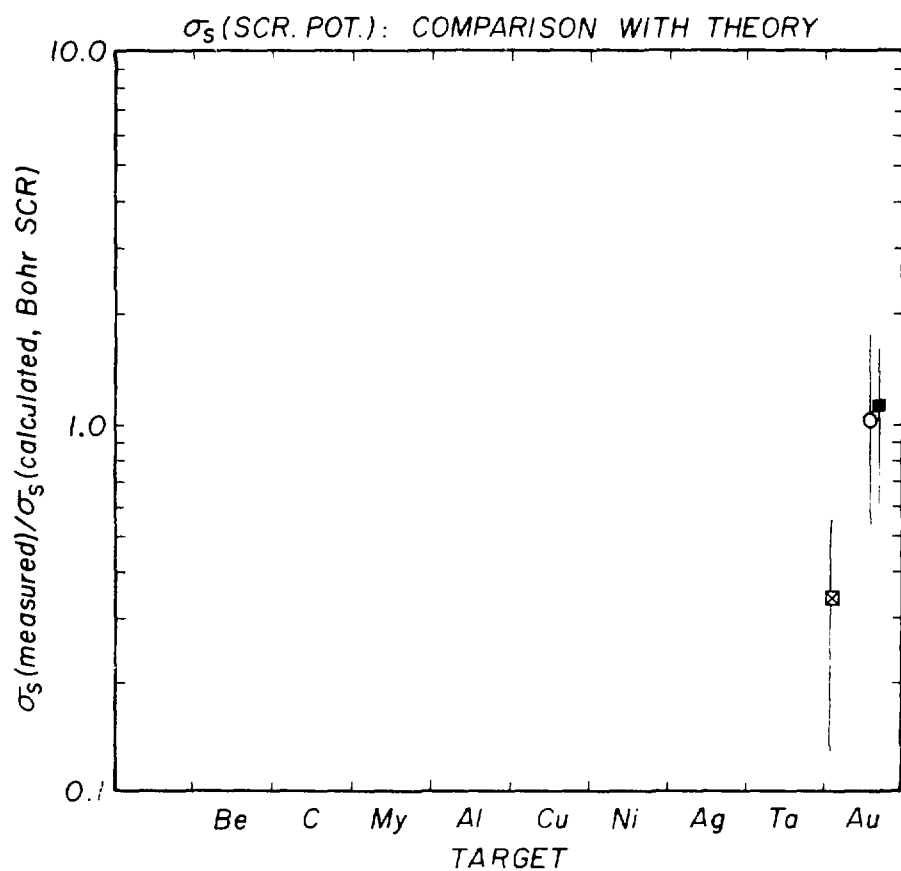
Fig. 14a



- ^{12}C at 250 MeV/nucleon
- ^{12}C 400 "
- ▲ ^{20}Ne 250 "
- ▤ ^{20}Ne 400 "
- ^{20}Ne 1050 "
- ^{20}Ne 2100 "
- △ ^{40}Ar 400 "
- ▨ ^{40}Ar 1050 "

XBL 804-9251

Fig. 14b



XBL 804-9252

Fig. 15

APPENDIX 1			
PROJECTILE 12C AT 140. MEV/AMU EYA(B) .83 +/- .10 EYA(SEN) 1.27 +/- .19 X10-5.			
TARGET BE	R 2.59 +/- .62X10 -7	X (AT/CM2) 2.941E+20 +/- 1.337E+19	THK (MG/CM2) 4.40 +/- .20
TARGET AL	R 1.83 +/- .22X10 -7 5.01 +/- .92X10 -7	X (AT/CM2) 1.272E+18 +/- 2.232E+17 2.545E+19 +/- 1.116E+18	THK (MG/CM2) 1.06 +/- .01 1.14 +/- .05
TARGET CJ	R 1.73 +/- .31X10 -6	X (AT/CM2) 1.327E+19 +/- 1.327E+18	THK (MG/CM2) 1.40 +/- .14
TARGET AU	R 4.53 +/- .09X10 -6 5.51 +/- .90X10 -6	X (AT/CM2) 1.284E+18 +/- 3.058E+17 1.193E+19 +/- 1.835E+18	THK (MG/CM2) 1.42 +/- .13 3.90 +/- .60
PROJECTILE 12C AT 250. MEV/AMU EYA(B) .82 +/- .05 EYA(SEN) 8.93 +/- .90 X10-5.			
TARGET BE	R 5.64 +/- .64X10 -8 5.64 +/- .64X10 -8	X (AT/CM2) 2.941E+20 +/- 1.337E+19 9.426E+20 +/- 4.011E+19	THK (MG/CM2) 4.40 +/- .20 14.10 +/- .60
TARGET C	R 1.25 +/- .11X10 -5 1.75 +/- .20X10 -6 2.62 +/- .18X10 -6	X (AT/CM2) 2.510E+16 +/- 1.004E+16 5.019E+18 +/- 2.008E+18 7.529E+18 +/- 2.510E+18	THK (MG/CM2) 1.05 +/- .02 1.10 +/- .04 1.15 +/- .05
TARGET MY	R 4.60 +/- .53X10 -8 4.60 +/- .53X10 -8	X (AT/CM2) 3.009E+18 +/- 1.254E+17 9.528E+18 +/- 3.134E+17	THK (MG/CM2) 1.48 +/- .02 1.52 +/- .05
TARGET AL	R 1.46 +/- .12X10 -8 2.75 +/- .25X10 -8 2.93 +/- .09X10 -8 3.09 +/- .13X10 -8 4.39 +/- .55X10 -8 4.35 +/- .55X10 -8	X (AT/CM2) 1.272E+18 +/- 2.232E+17 2.456E+18 +/- 2.232E+17 3.728E+18 +/- 4.465E+17 4.465E+18 +/- 2.232E+17 2.545E+19 +/- 1.116E+18 5.090E+19 +/- 2.232E+18	THK (MG/CM2) 1.06 +/- .01 1.11 +/- .01 1.17 +/- .02 1.20 +/- .01 1.14 +/- .05 2.28 +/- .10
TARGET CU	R 1.41 +/- .16X10 -7 1.41 +/- .16X10 -7 1.41 +/- .16X10 -7	X (AT/CM2) 3.602E+18 +/- 2.844E+17 6.635E+18 +/- 9.479E+17 2.180E+19 +/- 2.844E+18	THK (MG/CM2) 1.38 +/- .03 1.76 +/- .10 2.30 +/- .30
TARGET NI	R 1.41 +/- .16X10 -7	X (AT/CM2) 5.088E+19 +/- 1.026E+18	THK (MG/CM2) 4.96 +/- .10
TARGET YA	R 4.48 +/- .51X10 -7	X (AT/CM2) 6.990E+19 +/- 3.329E+18	THK (MG/CM2) 21.00 +/- 1.00
TARGET AU	R 4.85 +/- .56X10 -7 4.85 +/- .56X10 -7 4.85 +/- .56X10 -7	X (AT/CM2) 1.284E+18 +/- 3.058E+17 2.569E+18 +/- 6.116E+17 1.193E+19 +/- 1.835E+18	THK (MG/CM2) 1.42 +/- .10 1.84 +/- .20 3.90 +/- .60

XBL 804-9246

APPENDIX 1

PROJECTILE 12C AT 400. MEV/AMU				ETA(15)	.87 +/- .05	ETA(5EM)	3.70 +/- .37	XIG-3.
TARGET BE	R	X (AT/CM2)	THK (MG/CM2)					
	4.21 +/- .57X10 -8	2.941E+20 +/- 1.337E+19	4.40 +/- .20					
	4.21 +/- .57X10 -8	9.426E+20 +/- 4.011E+19	14.10 +/- .60					
TARGET C	R	X (AT/CM2)	THK (MG/CM2)					
	10.0 +/- .82X10 -9	5.019E+18 +/- 2.008E+18	.10 +/- .04					
	2.50 +/- .32X10 -8	9.235E+20 +/- 5.019E+19	18.40 +/- 1.00					
TARGET MY	R	X (AT/CM2)	THK (MG/CM2)					
	2.51 +/- .14X10 -8	3.009E+18 +/- 1.254E+17	.48 +/- .02					
	3.19 +/- .40X10 -8	2.044E+19 +/- 8.145E+17	3.26 +/- .13					
TARGET AL	R	X (AT/CM2)	THK (MG/CM2)					
	6.40 +/- .71X10 -9	1.272E+18 +/- 2.232E+17	.06 +/- .01					
	1.50 +/- .12X10 -8	2.456E+18 +/- 2.232E+17	.11 +/- .01					
	1.56 +/- .18X10 -8	4.465E+18 +/- 2.232E+17	.20 +/- .01					
	2.23 +/- .30X10 -8	2.545E+19 +/- 1.135E+18	1.14 +/- .05					
TARGET CU	R	X (AT/CM2)	THK (MG/CM2)					
	3.83 +/- .08X10 -8	3.602E+18 +/- 2.844E+17	.38 +/- .03					
	4.26 +/- .51X10 -8	1.327E+19 +/- 1.327E+18	1.40 +/- .14					
TARGET AG	R	X (AT/CM2)	THK (MG/CM2)					
	7.49 +/- .92X10 -8	1.200E+19 +/- 1.117E+18	2.15 +/- .20					
TARGET YA	R	X (AT/CM2)	THK (MG/CM2)					
	1.39 +/- .18X10 -7	6.990E+19 +/- 3.329E+18	21.00 +/- 1.00					
TARGET AU	R	X (AT/CM2)	THK (MG/CM2)					
	1.60 +/- .20X10 -7	1.284E+18 +/- 3.353E+17	.42 +/- .10					
	1.60 +/- .20X10 -7	1.193E+19 +/- 1.335E+18	3.90 +/- .60					
PROJECTILE 20NE AT 250. MEV/AMU				ETA(15)	.77 +/- .10	ETA(5EM)	7.87 +/- .80	XIG-5.
TARGET BE	R	X (AT/CM2)	THK (MG/CM2)					
	1.91 +/- .22X10 -6	2.941E+20 +/- 1.337E+19	4.40 +/- .20					
	1.91 +/- .22X10 -6	9.426E+20 +/- 4.011E+19	14.10 +/- .60					
	1.91 +/- .22X10 -6	1.477E+21 +/- 6.665E+19	22.10 +/- 1.00					
TARGET MY	R	X (AT/CM2)	THK (MG/CM2)					
	1.31 +/- .03X10 -6	6.519E+18 +/- 1.891E+17	1.0 +/- .03					
	1.47 +/- .05X10 -6	1.304E+19 +/- 3.34E+17	2.08 +/- .05					
TARGET AL	R	X (AT/CM2)	THK (MG/CM2)					
	7.80 +/- .16X10 -7	4.465E+18 +/- 2.232E+17	.20 +/- .01					
	1.31 +/- .03X10 -6	1.942E+19 +/- 2.232E+18	.87 +/- .10					
	1.36 +/- .15X10 -6	5.258E+19 +/- 4.465E+18	2.40 +/- .20					
	1.36 +/- .15X10 -6	2.545E+19 +/- 1.135E+18	1.14 +/- .05					
TARGET NI	R	X (AT/CM2)	THK (MG/CM2)					
	4.26 +/- .48X10 -6	5.088E+19 +/- 1.026E+18	4.56 +/- .10					
	4.26 +/- .48X10 -6	1.016E+20 +/- 2.052E+18	9.90 +/- .20					
TARGET TA	R	X (AT/CM2)	THK (MG/CM2)					
	1.27 +/- .15X10 -5	6.990E+19 +/- 3.329E+18	21.00 +/- 1.00					

XBL 894-9247

APPENDIX 1

PROJECTILE	ZONE AT 400 KEV/MPJ	ETA(B)	.85 +/- .10	ETA(SEM)	2.86 +/- .30 X10-4.
TARGET BE	R	X (AT/CM2)	THK (MG/CM2)		
	7.87 +/- .16X10 -7	2.941E+20 +/- 1.337E+19	4.40 +/- .20		
	7.87 +/- .16X10 -7	9.426E+20 +/- 4.011E+19	14.10 +/- .60		
TARGET MY	R	X (AT/CM2)	THK (MG/CM2)		
	4.94 +/- .10X10 -7	6.515E+18 +/- 1.881E+17	1.04 +/- .03		
	6.22 +/- .14X10 -7	1.304E+19 +/- 3.134E+17	2.08 +/- .05		
TARGET AL	R	X (AT/CM2)	THK (MG/CM2)		
	1.82 +/- .11X10 -7	4.465E+18 +/- 2.252E+17	.20 +/- .01		
	3.44 +/- .20X10 -7	1.942E+19 +/- 2.232E+18	.87 +/- .10		
	4.27 +/- .97X10 -7	2.545E+19 +/- 2.232E+18	1.14 +/- .10		
	4.27 +/- .97X10 -7	5.090E+19 +/- 3.349E+18	2.28 +/- .15		
	4.27 +/- .97X10 -7	5.358E+19 +/- 4.465E+18	2.40 +/- .20		
TARGET NI	R	X (AT/CM2)	THK (MG/CM2)		
	6.39 +/- 1.45X10 -7	5.088E+19 +/- 1.026E+18	4.96 +/- .10		
	6.39 +/- 1.45X10 -7	1.016E+20 +/- 2.052E+18	9.90 +/- .20		
TARGET TA	R	X (AT/CM2)	THK (MG/CM2)		
	2.40 +/- .54X10 -6	6.990E+19 +/- 3.329E+18	21.00 +/- 1.00		
	2.40 +/- .54X10 -6	1.398E+20 +/- 6.657E+18	42.00 +/- 2.00		
PROJECTILE	ZONE AT 1050 KEV/MPJ	ETA(B)	.82 +/- .35	ETA(SEM)	1.43 +/- .15 X10-4.
TARGET BE	R	X (AT/CM2)	THK (MG/CM2)		
	1.69 +/- .21X10 -7	2.941E+20 +/- 1.337E+19	4.40 +/- .20		
	1.69 +/- .21X10 -7	9.426E+20 +/- 4.011E+19	14.10 +/- .60		
TARGET C	R	X (AT/CM2)	THK (MG/CM2)		
	1.64 +/- .03X10 -8	5.019E+18 +/- 2.008E+18	.10 +/- .04		
	1.19 +/- .13X10 -7	9.235E+20 +/- 5.019E+19	18.40 +/- 1.00		
TARGET W	R	X (AT/CM2)	THK (MG/CM2)		
	6.40 +/- .13X10 -8	3.009E+18 +/- 1.254E+17	.48 +/- .02		
	10.0 +/- .20X10 -8	6.019E+18 +/- 1.961E+17	.96 +/- .03		
	1.16 +/- .02X10 -7	1.204E+19 +/- 3.134E+17	2.08 +/- .05		
	1.20 +/- .02X10 -7	2.044E+19 +/- 3.149E+17	3.76 +/- .13		
	1.20 +/- .02X10 -7	4.557E+19 +/- 1.881E+18	7.20 +/- .30		
TARGET AL	R	X (AT/CM2)	THK (MG/CM2)		
	9.35 +/- .95X10 -9	1.272E+18 +/- 2.232E+17	.06 +/- .01		
	1.64 +/- .15X10 -8	2.456E+18 +/- 2.232E+17	.11 +/- .01		
	2.58 +/- .14X10 -8	3.728E+18 +/- 4.465E+17	.17 +/- .02		
	2.87 +/- .27X10 -8	4.465E+18 +/- 2.232E+17	.20 +/- .01		
	4.82 +/- .17X10 -8	8.193E+18 +/- 6.647E+17	.37 +/- .03		
	7.02 +/- .80X10 -8	1.545E+19 +/- 1.116E+18	1.14 +/- .05		
TARGET CJ	R	X (AT/CM2)	THK (MG/CM2)		
	4.17 +/- .08X10 -8	3.602E+18 +/- 2.844E+17	.36 +/- .03		
	5.65 +/- .02X10 -8	1.327E+19 +/- 1.527E+18	1.40 +/- .14		
TARGET NI	R	X (AT/CM2)	THK (MG/CM2)		
	5.91 +/- .65X10 -8	5.088E+19 +/- 1.026E+18	4.96 +/- .10		
TARGET AG	R	X (AT/CM2)	THK (MG/CM2)		
	6.76 +/- .74X10 -8	1.200E+19 +/- 1.117E+18	2.15 +/- .20		
TARGET TA	R	X (AT/CM2)	THK (MG/CM2)		
	1.08 +/- .11X10 -7	6.990E+19 +/- 3.329E+18	21.00 +/- 1.00		
TARGET AU	R	X (AT/CM2)	THK (MG/CM2)		
	1.01 +/- .05X10 -7	1.284E+18 +/- 1.058E+17	.11 +/- .10		
	1.18 +/- .14X10 -7	1.193E+19 +/- 1.835E+18	3.90 +/- .60		

XBL 804-9248

APPENDIX 1

PROJECTILE 250 AT 2100. MEV/CMU				ETA(1)	ETA(2)	ETA(3)	ETA(4)
TARGET BE				R	X (AT/CM2)	THK (MG/CM2)	
6.73 +/- .18X10 -8				2.941E+20 +/- 1.537E+19	4.40 +/- .20		
6.73 +/- .18X10 -8				9.426E+20 +/- 4.911E+19	14.10 +/- .60		
TARGET C				R	X (AT/CM2)	THK (MG/CM2)	
5.80 +/- .6CX10 -9				5.019E+18 +/- 2.908E+18	.10 +/- .04		
4.92 +/- .10X10 -8				9.235E+20 +/- 5.015E+19	18.40 +/- 1.00		
TARGET MY				R	X (AT/CM2)	THK (MG/CM2)	
2.14 +/- .16X10 -8				3.009E+18 +/- 1.254E+17	.48 +/- .02		
3.18 +/- .19X10 -8				6.018E+18 +/- 1.881E+17	.96 +/- .03		
5.21 +/- .11X10 -8				2.044E+19 +/- 8.149E+17	3.26 +/- .13		
5.27 +/- .01X10 -8				4.557E+19 +/- 1.881E+18	7.27 +/- .30		
TARGET AL				R	X (AT/CM2)	THK (MG/CM2)	
2.32 +/- .69X10 -9				1.272E+19 +/- 2.232E+17	.06 +/- .01		
5.95 +/- .95X10 -9				2.456E+18 +/- 2.232E+17	.11 +/- .01		
8.04 +/- .63X10 -9				4.465E+18 +/- 2.232E+17	.20 +/- .01		
2.67 +/- .31X10 -8				2.545E+19 +/- 1.116E+18	1.14 +/- .05		
TARGET CU				R	X (AT/CM2)	THK (MG/CM2)	
1.28 +/- .10X10 -8				3.602E+18 +/- 2.844E+17	.38 +/- .03		
1.75 +/- .21X10 -8				1.687E+19 +/- 1.895E+18	1.78 +/- .20		
TARGET TA				P	X (AT/CM2)	THK (MG/CM2)	
1.84 +/- .13X10 -8				6.590E+19 +/- 3.329E+18	21.00 +/- 1.00		
TARGET AJ				R	X (AT/CM2)	THK (MG/CM2)	
1.61 +/- .13X10 -8				1.284E+18 +/- 3.059E+17	.42 +/- .10		
1.94 +/- .23X10 -8				1.193E+19 +/- 1.335E+18	3.90 +/- .60		
PROJECTILE 400 AT 400. MEV/CMU				ETA(1)	ETA(2)	ETA(3)	ETA(4)
TARGET BE				R	X (AT/CM2)	THK (MG/CM2)	
2.63 +/- .05X10 -5				2.941E+20 +/- 1.537E+19	4.40 +/- .20		
3.12 +/- .24X10 -5				9.426E+20 +/- 4.911E+19	14.10 +/- .60		
TARGET C				R	X (AT/CM2)	THK (MG/CM2)	
1.62 +/- .24X10 -6				5.019E+18 +/- 2.908E+18	.10 +/- .04		
2.33 +/- .25X10 -5				9.235E+20 +/- 5.015E+19	18.40 +/- 1.00		
TARGET MY				R	X (AT/CM2)	THK (MG/CM2)	
6.61 +/- .14X10 -6				3.009E+18 +/- 1.254E+17	.48 +/- .02		
1.27 +/- .02X10 -5				6.018E+18 +/- 1.881E+17	.96 +/- .03		
1.77 +/- .04X10 -5				1.304E+19 +/- 3.134E+17	2.08 +/- .05		
2.07 +/- .24X10 -5				2.044E+19 +/- 8.149E+17	3.26 +/- .13		
2.27 +/- .25X10 -5				4.557E+19 +/- 1.881E+18	7.27 +/- .30		
2.27 +/- .25X10 -5				6.601E+19 +/- 2.507E+18	10.53 +/- .40		
TARGET AL				R	X (AT/CM2)	THK (MG/CM2)	
1.29 +/- .04X10 -6				1.272E+18 +/- 2.232E+17	.06 +/- .01		
2.08 +/- .10X10 -6				2.456E+18 +/- 2.232E+17	.11 +/- .01		
3.06 +/- .06X10 -6				4.465E+18 +/- 2.232E+17	.20 +/- .01		
1.11 +/- .02X10 -5				2.545E+19 +/- 1.116E+18	1.14 +/- .05		
1.44 +/- .05X10 -5				5.040E+19 +/- 2.232E+18	2.28 +/- .10		
TARGET CU				R	X (AT/CM2)	THK (MG/CM2)	
1.14 +/- .06X10 -5				3.602E+18 +/- 2.844E+17	.38 +/- .03		
2.13 +/- .28X10 -5				1.327E+19 +/- 1.327E+18	1.40 +/- .14		
TARGET III				R	X (AT/CM2)	THK (MG/CM2)	
2.04 +/- .23X10 -5				5.088E+19 +/- 1.026E+18	4.96 +/- .10		
TARGET AG				R	X (AT/CM2)	THK (MG/CM2)	
4.27 +/- .46X10 -5				1.200E+19 +/- 1.117E+18	2.15 +/- .20		
TARGET TA				R	X (AT/CM2)	THK (MG/CM2)	
6.92 +/- .77X10 -5				6.99CE+19 +/- 3.329E+18	21.00 +/- 1.00		
TARGET AJ				R	X (AT/CM2)	THK (MG/CM2)	
5.57 +/- .11X10 -5				1.284E+18 +/- 3.059E+17	.42 +/- .10		
8.08 +/- .90X10 -5				1.193E+19 +/- 1.335E+18	3.90 +/- .60		

XBL 804-9249

APPENDIX 1

PROJECTILE	45AR AT 1050 MEV/KMU	ETL(B)	.83 +/- .05	ETA(SEM)	4.00 +/- .40 X10-4.
TARGET BE	R	X (AT/CM2)	THK (MG/CM2)		
	5.22+/- .10X10 -6	2.941E+20+/-1.337E+19	4.40+/- .20		
	6.36+/- .09X10 -6	9.426E+20+/-4.011E+19	14.10+/- .60		
TARGET C	R	X (AT/CM2)	THK (MG/CM2)		
	2.23+/- .15X10 -7	5.019E+18+/-2.003E+18	.10+/- .04		
	4.75+/- .53X10 -6	9.235E+20+/-5.019E+19	18.40+/-1.00		
TARGET MY	R	X (AT/CM2)	THK (MG/CM2)		
	1.04+/- .02X10 -6	3.009E+18+/-1.254E+17	.46+/- .02		
	2.03+/- .04X10 -6	6.018E+18+/-1.881E+17	.96+/- .03		
	4.24+/- .08X10 -6	2.044E+19+/-9.149E+17	3.26+/- .13		
	4.09+/- .20X10 -6	2.345E+19+/-9.403E+17	3.74+/- .15		
	4.92+/- .53X10 -6	9.115E+19+/-3.761E+18	14.54+/- .60		
TARGET AL	R	X (AT/CM2)	THK (MG/CM2)		
	3.83+/- .08X10 -7	3.728E+18+/-4.465E+17	.17+/- .02		
	1.83+/- .04X10 -6	2.545E+19+/-1.116E+18	1.14+/- .05		
	2.53+/- .05X10 -6	5.590E+19+/-2.232E+18	2.23+/- .10		
	2.90+/- .06X10 -6	7.635E+19+/-3.549E+18	3.42+/- .15		
TARGET CJ	R	X (AT/CM2)	THK (MG/CM2)		
	7.50+/- .15X10 -7	3.607E+18+/-2.844E+17	.38+/- .03		
	1.61+/- .23X10 -6	1.327E+19+/-1.227E+18	1.40+/- .14		
TARGET NJ	R	X (AT/CM2)	THK (MG/CM2)		
	1.76+/- .23X10 -6	5.088E+19+/-1.026E+18	4.96+/- .10		
TARGET AG	R	X (AT/CM2)	THK (MG/CM2)		
	1.98+/- .04X10 -6	1.200E+19+/-1.117E+18	2.15+/- .20		
TARGET AJ	R	X (AT/CM2)	THK (MG/CM2)		
	2.27+/- .05X10 -6	1.284E+18+/-3.059E+17	.42+/- .10		
	3.52+/- .39X10 -6	1.193E+19+/-1.855E+18	5.90+/- .60		

XBL 804-9250